AD-A127 946 A LIGHT-SCATTERING SYSTEM TO MEASURE CAVITATION NUCLEI: 1/2
ANALYSIS AND CALI..(U) PENNSYLVANIA STATE UNIV
UNIVERSITY PARK APPLIED RESEARCH LAB.. C B YUNGKURTH
UNCLASSIFIED 30 SEP 82 ARL/PSU/TM-82-204 F/G 20/6 NL

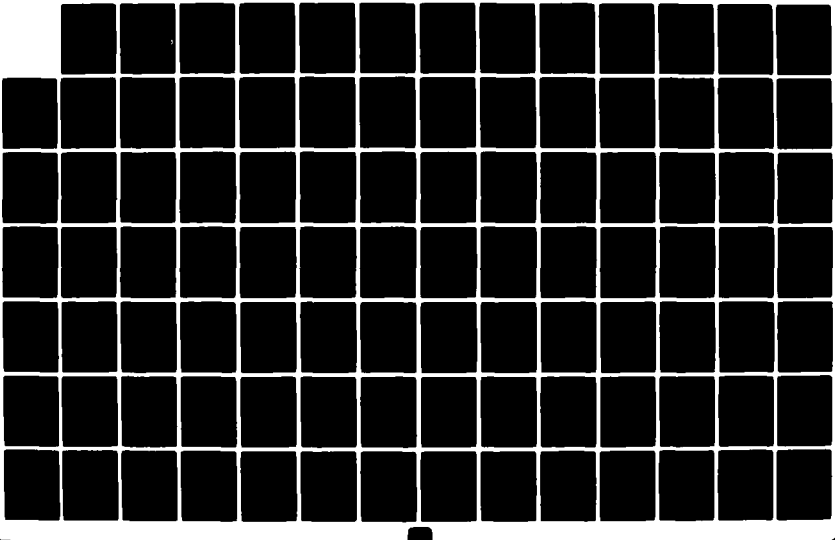

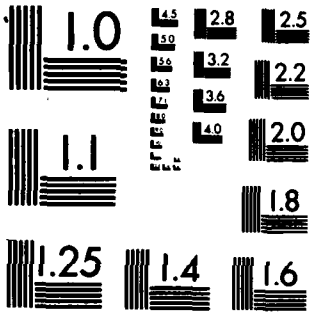

MICROCOPY RESOLUTION TEST CHART
NATIONAL BUREAU OF STANDARDS-1963-A

6

A LIGHT-SCATTERING SYSTEM TO MEASURE CAVITATION NUCLEI: ANALYSIS AND CALIBRATION

C. B. Yungkurth

AD A127946

Technical Memorandum
File No. TM 82-204
30 September 1982
Contract No. N00024-79-C-6043

Copy No. //

DTIC
ELECTE
MAY 6 1983
D
H

The Pennsylvania State University
APPLIED RESEARCH LABORATORY
Post Office Box 30
State College, PA 16801

Approved for Public Release
Distribution Unlimited

NAVY DEPARTMENT

NAVAL SEA SYSTEMS COMMAND

DTIC FILE COPY

83 05 06-006

SECURITY CLASSIFICATION OF THIS PAGE (When Data Entered)

REPORT DOCUMENTATION PAGE		READ INSTRUCTIONS BEFORE COMPLETING FORM
1. REPORT NUMBER TM 82-204	2. GOVT ACCESSION NO.	3. RECIPIENT'S CATALOG NUMBER
4. TITLE (and Subtitle) A LIGHT-SCATTERING SYSTEM TO MEASURE CAVITATION NUCLEI: ANALYSIS AND CALIBRATION		5. TYPE OF REPORT & PERIOD COVERED Technical Memorandum 6. PERFORMING ORG. REPORT NUMBER
7. AUTHOR(s) C. B. Yungkurth		8. CONTRACT OR GRANT NUMBER(s) N00024-79-C-6043
9. PERFORMING ORGANIZATION NAME AND ADDRESS Applied Research Laboratory Post Office Box 30 State College, PA 16801		10. PROGRAM ELEMENT, PROJECT, TASK AREA & WORK UNIT NUMBERS
11. CONTROLLING OFFICE NAME AND ADDRESS Naval Sea Systems Command Washington, DC 20362 Code NSEA-63R31		12. REPORT DATE 30 September 1982 13. NUMBER OF PAGES 116
14. MONITORING AGENCY NAME & ADDRESS(if different from Controlling Office)		15. SECURITY CLASS. (of this report) UNCLASSIFIED 15a. DECLASSIFICATION/DOWNGRADING SCHEDULE

16. DISTRIBUTION STATEMENT (of this Report)

Approved for public release. Distribution unlimited
Per NAVSEA - Oct. 28, 1982.

17. DISTRIBUTION STATEMENT (of the abstract entered in Block 20, if different from Report)

18. SUPPLEMENTARY NOTES

19. KEY WORDS (Continue on reverse side if necessary and identify by block number)

thesis, light, scattering, system, cavitation, nuclei

20. ABSTRACT (Continue on reverse side if necessary and identify by block number)

An investigation is made into the problem of measurement inaccuracies of a Light-Scattering System (LSS) that can be utilized to measure cavitation nuclei in terms of microbubble populations. The principle of the system whereby the magnitude of scattered light from an incident laser beam illuminating a microbubble is correlated with the microbubble size has been developed and demonstrated by A. Keller. However, the goal of this investigation is to increase the reliability of the LSS by minimizing several of the inaccuracies. →

DD FORM 1 JAN 73 1473 EDITION OF 1 NOV 65 IS OBSOLETE

SECURITY CLASSIFICATION OF THIS PAGE (When Data Entered)

20. Modifications to the LSS are proposed to minimize system inaccuracies. One is a dual-detector signal analysis system to facilitate the screening out of solid particulate or non-microbubble nuclei from the total nuclei distribution being measured. The other is a mathematical technique called an inversion scheme used to correct inaccurate nuclei count rates reported by the system due to the Probe Volume not having a uniform light intensity distribution.

Results are presented from a series of rigorous experiments conducted to test the effectiveness of the proposed modifications. In these experiments, the modified LSS is used to measure many different nuclei distributions in a highly controlled environment with a holography system being used to calibrate the LSS test results. An additional series of experiments is conducted to obtain direct measurements of the laser light intensity distribution in the measurement Probe Volume.

Analysis of the results shows that the proposed modifications are relevant for the inaccuracies discussed, but that a problem of nuclei counting statistics must still be dealt with before the system can be optimized.

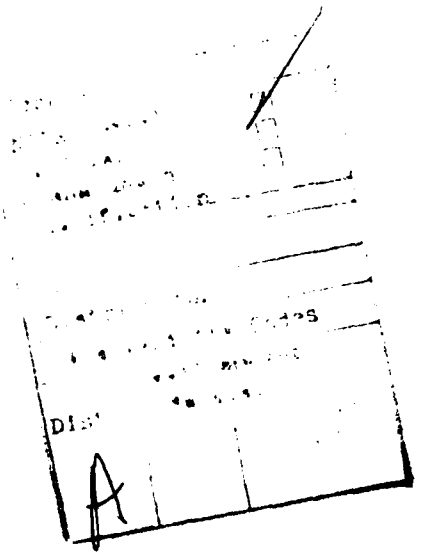

DTIC
INSPECTED

ABSTRACT

An investigation is made into the problem of measurement inaccuracies of a Light-Scattering System (LSS) that can be utilized to measure cavitation nuclei in terms of microbubble populations. The principle of the system whereby the magnitude of scattered light from an incident laser beam illuminating a microbubble is correlated with the microbubble size has been developed and demonstrated by A. Keller. However, the goal of this investigation is to increase the reliability of the LSS by minimizing several of the inaccuracies.

Modifications to the LSS are proposed to minimize system inaccuracies. One is a dual-detector signal analysis system to facilitate the screening out of solid particulate or non-microbubble nuclei from the total nuclei distribution being measured. The other is a mathematical technique called an inversion scheme used to correct inaccurate nuclei count rates reported by the system due to the Probe Volume not having a uniform light intensity distribution.

Results are presented from a series of rigorous experiments conducted to test the effectiveness of the proposed modifications. In these experiments, the modified LSS is used to measure many different nuclei distributions in a highly controlled environment with a holography system being used to calibrate the LSS test results. An additional series of experiments is conducted to obtain direct measurements of the laser light intensity distribution in the measurement Probe Volume.

Analysis of the results shows that the proposed modifications are relevant for the inaccuracies discussed, but that a problem of

nuclei counting statistics must still be dealt with before the system can be optimized.

TABLE OF CONTENTS

Page

LIST OF TABLES

LIST OF FIGURES

NOMENCLATURE

a_n, b_n	Mie scattering coefficients (A.1)
A	voltage amplitude of signal pulse (B.1)
C	nuclei count rate (B.3)
C_i	column matrix of signal count rates in the range of A_i to $A_i + \Delta A_i$ (B.4)
C_t	average total rate of nuclei passing through the Probe Volume (3.1)
d	diameter of nuclei
d_{max}	diameter of largest nuclei size in the range considered (3.3)
d_{min}	diameter of smallest nuclei size in the range considered (3.3)
$\vec{E}_\theta, \vec{E}_\phi$	components of scattered electric field vector (A.20)
$F(d,\Omega)$	scattering response function (B.1)
G_i	gain of the photomultiplier and associated electronics (B.1)
H	dimensionless function, varying between 0 and 1, and describing the transfer of scattered light from the PV to the photomultiplier (B.2)
I	wave vector intensity (A.22)
I_0	intensity of the laser light in the PV (B.1)
i,j,k,l	matrix indices
k	wave number (A.1)
n	nuclei concentration
n_T	total nuclei concentration (3.3)
N_j	column matrix of nuclei concentrations for nuclei in the size range F_j to $F_j + \Delta F_j$ (B.4)
N_m	concentration of a nuclei size, d_{max}, from the largest size class in the Pulse-Height Analyzer (B.8)

NOMENCLATURE (continued)

$n_{(r)}$	size concentration distribution, as a function of nuclei size (3.4)
m	complex refractive index (A.12)
$N_{dust\ rejected}$	number of non-symmetric particles rejected by the PHC (5.2)
N_{dust}	total number of non-symmetric particles encountered by the Pulse-Height Comparator (5.2)
$N_{spheres\ rejected}$	number of calibration sphere nuclei rejected by the PHC (5.3)
$N_{spheres}$	total number of calibration sphere nuclei encountered by the PHC (5.3)
M	composition ratio of a nuclei population (5.6)
P(k,x)	Poisson probability density function (3.1)
P_{int}	probability of interference (3.2)
$P_n(\cos\theta)$	Legendre polynomials (A.4)
PV	Probe Volume
PHA	Pulse-Height Analyzer
PHC	Pulse-Height Comparator
r	nuclei radius
R	asymmetry ratio of scattering (Section 3.2.2)
$\overline{R}$	average asymmetry ratio (Section 3.2.2)
R_c	cutoff asymmetry ratio (Section 3.2.2)
$R(\rho)$	radial separation variable (A.2)
R_{dust}	ratio of $N_{dust\ rejected}$ to N_{dust} (5.2)
$R_{composite}$	ratio of the total number of nuclei rejected by the PHC to the total number of nuclei encountered by the PHC (5.3)
R_{sphere}	ratio of $N_{spheres}$ rejected to $N_{spheres}$ (5.4)

NOMENCLATURE (continued)

S	area of the PV normal to the flow direction (B.3)
S_{ij}	$S(A_i,F_j)$ = equivalent cross-sectional area of the PV which yields normalized amplitudes in the range, A_i to $A_i + \Delta A_i$, for the nuclei having normalized response functions in the range, F_j to $F_j + \Delta F_j$ (B.4)
S_{ij}^{-1}	the inverse matrix of S_{ij} (B.5)
SD	standard deviation of the asymmetry ratio (Section 3.2.2)
$S_1(\theta), S_2(\theta)$	complex amplitudes of the scattered wave (A.18)
U	bulk velocity of the flow (B.3)
V_m	Probe Volume size (3.3)
x	size parameter in scattering equations (A.12)
y,z	scattering coordinates transverse to the incident beam direction (B.2)
α	nuclei size parameter, defined same as x (B.1)
β	scale factor (4.1)
δ	phase difference between E_θ and E_ϕ (A.23)
$(\theta,\phi) = \Omega$	solid angle into which light is scattered (A.1, B.1)
λ	wave length of incident laser light (A.12)
π	a scalar component of a wave vector (A.1)
$\pi_n(\cos\theta)$	a form of Legendre polynomials (A.15)
ρ	radial distance from the scattering center to the point of observation (A.1)
τ	PM - tube resolving time, average length of time for nuclei to pass through the PV (3.1)
$\Theta(\theta)$	transverse separation variable (A.2)
$\Phi(\theta)$	aximuthal separation variable (A.2)
X_n, ψ_n, ζ_n	Ricatti-Bessel functions (A.3)

ACKNOWLEDGMENTS

The author wishes to express his appreciation to Dr. Michael L. Billet, on the research staff of the Garfield Thomas Water Tunnel, for his insightful guidance throughout the course of this investigation, and to Dr. J. William Holl, Professor of Aerospace Engineering, for his assistance in formulating the concept of the investigation.

The investigation was conducted at the Garfield Thomas Water Tunnel at The Pennsylvania State University under the sponsorship of the Applied Research Laboratory's Exploratory and Foundational Programs and the Naval Sea Systems Command, Code NSEA 63R-31.

Further appreciation is expressed to Dr. Chandra S. Vikram of the Materials Research Laboratory at The Pennsylvania State University for his invaluable assistance in utilizing the holography system and also to the many members of the Garfield Thomas Water Tunnel Staff whose assistance made the implementation of this investigation possible.

CHAPTER 1

INTRODUCTION

1.1 Background

Cavitation nuclei is the general name used to refer to the impurities which cause weak spots in a liquid, and thus prevent the liquid from supporting the amount of tension which theory would predict. It is this inability of a liquid to support a tension that leads to the phenomenon of cavitation.

Various forms of cavitation nuclei have been theorized, but all can be considered in one of two classes, depending on where they originate. Stream nuclei exist in the free-stream liquid in such forms as solid particulates or stabilized microbubbles. Surface nuclei originate in the surface of the fluid boundary, by means of cracks and crevices in the boundary. A significant effort has been devoted to studying the nature of these cavitation nuclei, and an excellent review of this research is given by Holl in Reference [1]. Although a qualitative relationship has been established between the presence of cavitation nuclei and the appearance of cavitation during experiments, progress in making quantitative predictions of such relationships has been dependent upon the ability to obtain measurements of cavitation nuclei properties such as shape, size distribution, and concentration. Therefore, much research has also been concerned with developing systems to obtain such measurements. Morgan [2] gives a summary of various methods employed to measure cavitation nuclei.

In investigating the cavitation phenomenon at ARL/PSU, progress was hampered by the need to measure the stream-type cavitation nuclei distribution during cavitation experiments. To remedy this, a system to obtain such measurements was developed, patterned after the method introduced by Keller [3]. This method was based on measuring the scattering of a laser light beam as nuclei moved through it, and was thus called a laser light-scattering system, often abbreviated as LSS.

The Keller system was chosen because it was believed to have the greatest potential for meeting the requirements deemed necessary in a system for measuring cavitation nuclei during experiments. These requirements arose because of the peculiar experimental conditions involved in cavitation research, and demand the following capabilities:

1. Obtain measurements in the flow environment itself, yet without disturbing it: It is a well-known fact that the occurrence of cavitation is highly sensitive to the geometry of the fluid boundary and the nature of the fluid flow itself. For this reason, the measurement system must not affect the fluid flow, yet it must be able to obtain measurements at the very specific locations on the fluid boundary where the cavitation occurs.
2. Obtain measurements on-line: It has also been shown that the cavitation nuclei distribution cannot be assumed to remain constant with respect to time, a phenomenon which has been linked to the lack of repeatability in cavitation experiments [5]. Therefore, in order to conduct meaningful investigations into this kind of phenomenon, the measurement

system must give information about the nuclei distributions which exist during cavitation experiments, i.e., on-line.

3. Separate measurements of solid particulate nuclei from gas bubble nuclei in the same flow: The necessity of this requirement became apparent after a series of experiments conducted jointly by the Applied Research Laboratory at Penn State University and the California Institute of Technology. One of the conclusions made from this effort was that differences in cavitation behavior in test facilities were attributable to the variation in the gas bubble fraction of the total nuclei population [6]. Thus, it was considered essential that a nuclei measurement system be able to screen out the solid particulate nuclei and examine only the gas bubble distribution.
4. Measure nuclei in the size range of 5 to 80 microns in diameter: Experience and theory have shown that stream-type nuclei which affect cavitation behavior are in this range.

As the Keller system was used in some recent experiments [4], it became clear that there were still some fundamental inaccuracies and uncertainties in the system's performance that would have to be defined and eliminated before it could be relied upon to give the kind of data needed to conduct further meaningful research into the cavitation phenomenon. For example, an attempt was made by Keller to distinguish between gas bubbles and solid particulates by subtracting distributions

obtained at high pressure from those at low pressure, essentially assuming that the gas bubble distribution will be eliminated at high pressure, leaving only the solid particulate distribution. This requires some basic knowledge of the statistics of the flow which are not generally known. In addition, the pressure cannot be increased high enough in most flow situations to apply this method. In any case, the use of this method reveals that the Keller system cannot distinguish bubbles and solid particulates independently.

Another major inaccuracy observed in the Keller method, as noted in Reference [4], is the tendency for gas bubble concentrations of a given radius to register counts not only in the distribution channel corresponding to that radius, but also in all channels lower than that radius. The overall effect is that the size distribution reported by the system is significantly different from the actual distribution.

1.2 Objectives of the Investigation

It was the intent of this investigation to set forth the principles involved in the LSS inaccuracies, to describe methods whereby these inaccuracies could be minimized or eliminated, and finally to implement these methods as modifications to the present LSS. This was to achieve the goal of providing a more reliable system for the measurement of cavitation nuclei.

In order to accomplish these objectives, the scope of this investigation covered the following issues:

1. The establishment of a criterion for determining the optimal size of the nuclei measurement region in the medium.

2. The development of a system which would be able to separate measurements of microbubble nuclei from measurements of solid particulate nuclei.
3. The utilization of a mathematical model to correct measured size distributions.

As an additional issue in the scope of this investigation, a method for correcting size distributions by means of direct measurements of the intensity distribution in the measurement region was developed.

The procedure of this investigation was to obtain the needed criteria and mathematical models primarily from existing theories and known principles of the system's operation, and then to conduct experiments that would verify those theories. The plan involved taking a large number of measurements of many different nuclei distributions, these using the original Keller system, a modified LSS system, and a holography system which would provide a calibration of the true nuclei distributions. Data from these experiments were then compared with predicted results in determining the optimal measurement region (or Probe Volume) size, and similarly for validating the method of separating bubble nuclei and solid particulate nuclei. This same data base was also used to both implement and validate the mathematical model to correct measured bubble size distributions.

The latter part of the experiments was to obtain measurements of the probe volume intensity distributions for several conditions, and then to correlate these measurements with measurements of the bubble size distribution taken simultaneously. This data base provided the

means for implementing and verifying the method of correcting bubble size distributions through direct measurement of Probe Volume intensity distributions.

CHAPTER 2

DESCRIPTION OF THE LIGHT-SCATTERING SYSTEM

2.1 The Keller System

2.1.1 Principle of Operation. The governing principle of this measurement system is dependent on the size regime of the nuclei being measured. Measurements in the micron size range dictate that the Mie scattering theory be used, since this is the theory relevant for nuclei whose sizes are on the same order of magnitude as the wave lengths of the laser light which illuminates them. However, for the measurement of the larger microbubbles, geometric theories could be utilized.

Mie theory predicts that a monochromatic, coherent, plane-wave light beam will be scattered in all directions by an arbitrary particle and that the intensity of that scattered light will depend strongly on the size, shape, and refractive index of the particle. The intensity will also vary greatly with the solid angle into which the light is scattered. For spherical particles, Mie theory predicts that in certain directions perpendicular to the illuminating beam direction, the scattered light intensity will increase monotonically for a limited particle size range and a given refractive index. It is this characteristic of the scattering theory which forms the basis of the measurement system, as shown in Figure 1. A derivation of this relationship is given in Appendix A.

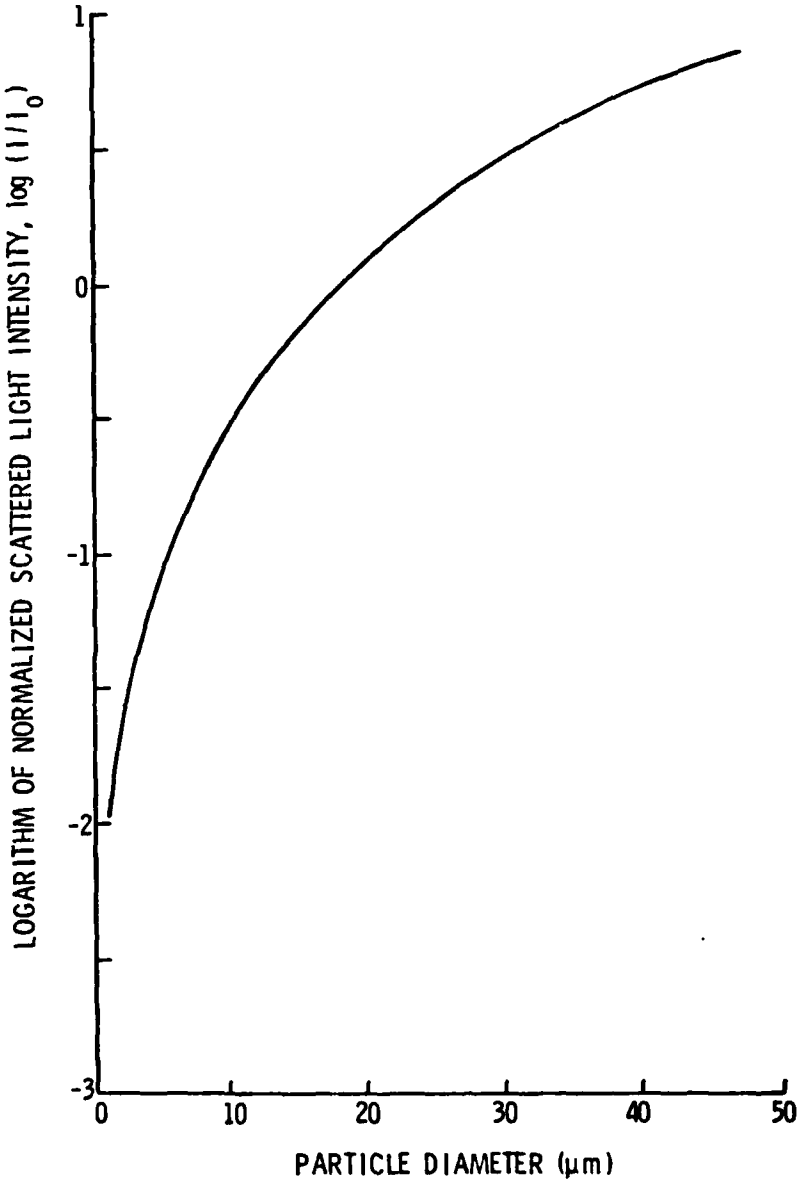

Figure 1a. Monotonic Relationship of Scattered Light Intensity With Nuclei Size in the ARL/PSU Light-Scattering System (LSS).

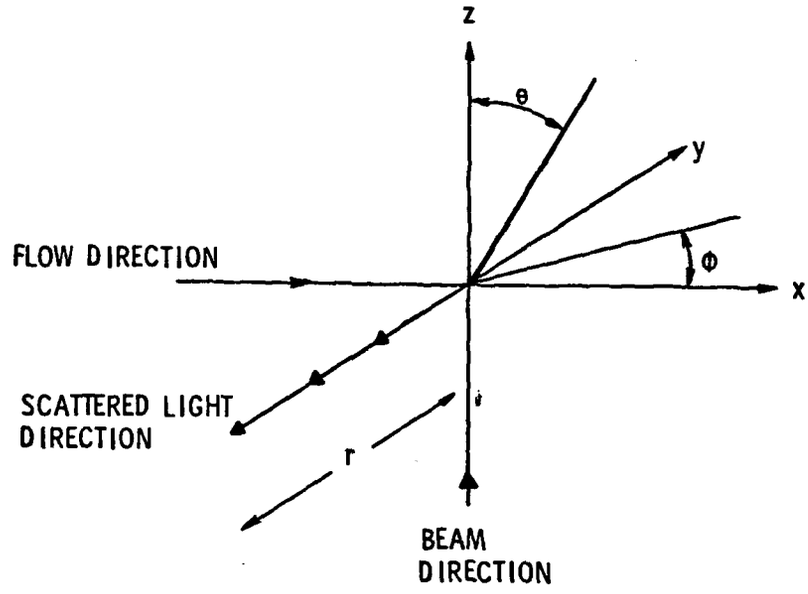

Figure 1b. Scattering Coordinate System for the ARL/PSU LSS.

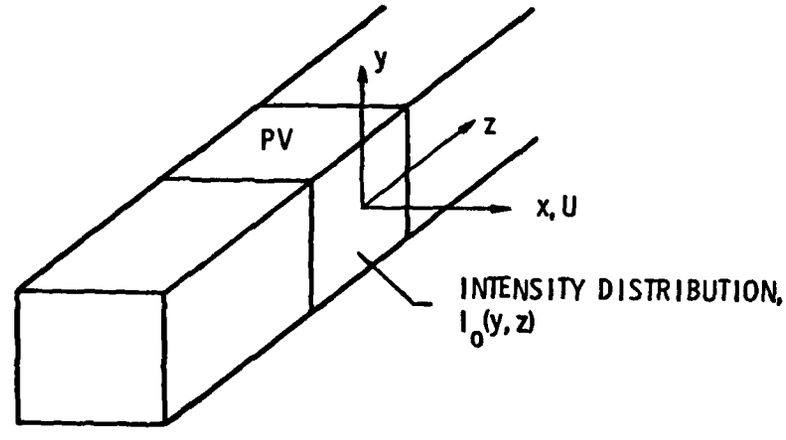

Figure 2. Simplified Representation of Probe Volume (PV) Dimensions.

2.1.2 Method of Operation. The actual cavitation nuclei measurement system, which is based on the Keller method, can be thought of as being composed of three primary subsystems:

1. Sensing subsystem - The purpose of the sensing subsystem is to construct a monochromatic, coherent, plane-wave light beam of known dimensions and intensity at a location in the flow where the nuclei distribution is desired to be measured (this location will hereafter be referred to as the Probe Volume (PV)). This purpose is achieved in the Keller system by passing the beam from a laser light source through the optical system, such as is shown in Figure 3. The primary issue in the sensing subsystem is to obtain a beam at the PV that has optimal intensity and physical dimensions so as to minimize statistical errors encountered when sampling large numbers of nuclei. The nature of these errors will be discussed further in Chapter 3.
2. Measuring subsystem - The purpose of the measuring subsystem is to record the amount of laser light which is scattered by a nucleus as it passes through the laser beam at the PV (the laser beam at the PV which illuminates the nuclei will often be referred to as the incident beam). The Keller system accomplishes this by using a photosensitive detector, or photomultiplier tube (abbreviated as PM-tube), to detect the intensity of scattered light. As seen in Figure 3, the scattered light is collected by a set of lenses whose diameter and focal length determine

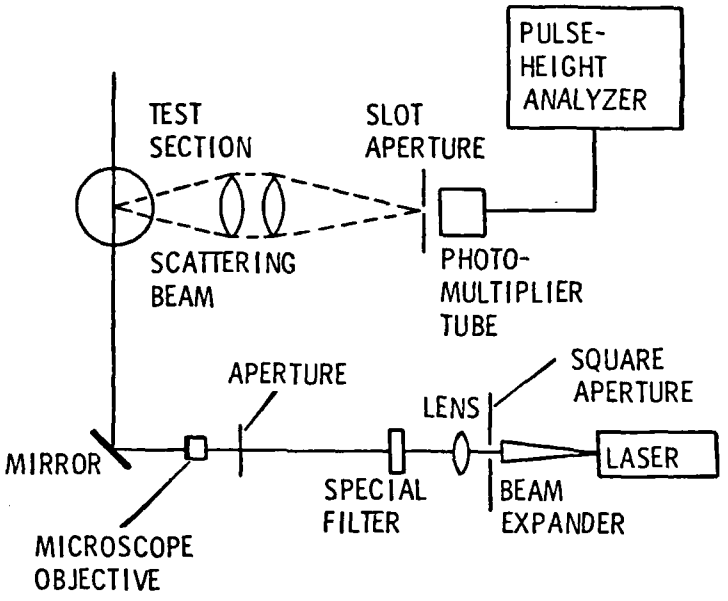

Figure 3. Schematic of the Keller LSS.

a fixed solid angle of scattered light to be collected. This light is then focused onto a slit aperture, which restricts the length of the laser beam monitored by the PM-tube. The PM-tube then converts the light scattered by individual nuclei into equivalent electrical signals. The slit aperture restricts the amount of light entering the PM-tube in order to set the third dimension of the laser light PV, the other two dimensions are set by the cross-sectional area of the incident beam (see Figure 2). The primary issues in this subsystem are the providing of a guarantee that the PM-tube is at the beam-perpendicular location shown to be optimal by the Mie theory, and optimization of the size of the slit aperture so as to minimize the statistical errors mentioned in the sensing subsystem.

3. Analyzing subsystem - The purpose of this subsystem is to accurately interpret the recordings of scattered laser light obtained over a fixed time interval, transforming the electrical signals from the measuring system into a histogram representing the nuclei size distribution which was present during that time interval. This is achieved in the Keller system by passing the electrical signals from the PM-tube into a device called a Pulse-Height Analyzer (PHA) to obtain the distribution histogram. The PHA is a device which can be thought of as the electronic equivalent of the scattering relationship

shown in Figure 1, with the difference being that the relationship between nuclei size and scattered light intensity is not continuous but is coarse-grained into discrete intervals, called PHA channels. The number and relative width of the PHA channels are arbitrary, being governed primarily by the degree of measurement accuracy desired. The primary issue in the analyzing subsystem is to interpret a large enough data base so as to minimize statistical errors, yet do it in a small enough time interval to still qualify the light-scattering system as an on-line measurement system.

2.2 Identifying System Inaccuracies

In this investigation the inaccuracies under consideration have their origin in each of the three subsystems detailed in Section 2.1.2. In the sensing subsystem, a need for a clearer definition of the size and shape of the PV was observed, so as to better understand the amount of error inherent in the nuclei distribution measurements. The confidence in the system's measurements is in direct proportion to the precision of the system's error estimate; thus, such a definition of the PV and the errors associated with it was deemed essential for a reliable measurement system.

The inability of the system to meet the requirement of distinguishing between microbubbles and solid particulates was traced back to an under-utilization of the scattered light signals as recorded by the measuring system.

A major inaccuracy was observed in the analyzing subsystem, whereby the final nuclei distribution reported by the PHA was consistently found to be significantly different from the actual distribution. Experiments done in Reference [7] showed that individual scattering from nuclei does repond in the manner predicted by the Mie theory, so it was concluded that the problem must be limited to the incident beam character itself in the sensing subsystem.

CHAPTER 3

PRINCIPLES OF INACCURACIES AND PROPOSED SOLUTIONS

3.1 The Criteria for the Probe Volume

3.1.1 Nature of Potential Errors. As was discussed, the size of the laser light Probe Volume (PV) is a source of potential inaccuracy in the light-scattering system (LSS). This inaccuracy arises because not all microbubbles of the same size which enter the PV will scatter the same amount of light. There are two mechanisms which can cause this departure from predicted scattering behavior: coincidence errors and illumination errors.

Measurement inaccuracy due to coincidence errors is usually caused by the smaller nuclei in the range of sizes being measured. If the PV is large enough, it is possible for more than one scatterer to be illuminated simultaneously by the laser, yet only a single composite light-intensity measurement is recorded by the photo-multiplier tube (PM-tube). The resulting measurement goes on to be interpreted as a single large nucleus, instead of several small ones, and an incorrect picture of the size distribution is obtained.

Inaccuracy due to illumination errors is caused by the scatterer in the PV not being illuminated by the peak intensity of the laser light. If the scatterer is large enough, it is also possible for it to pass through an "edge" of the PV so that only part is illuminated. Both of these situations cause the LSS to interpret the corresponding scatterer as being smaller than it actually is, again leading to an incorrect picture of the size distribution.

3.1.2 Coincidence Error Criterion. The objective of a coincidence error criterion is to establish a formula whereby the extent of inaccuracy in measurements due to coincidence effects can be calculated for a given set of experimental conditions. Any realistic probability model of the interaction of a scatterer with the PV must be based on the Poisson probability distribution, which gives the probability of k scatterers being simultaneously in the PV as

$$P(k,x) = \frac{x^k e^{-x}}{k!} \tag{3.1}$$

where $x = C_t \tau$

C_t = average total rate of scatterers passing through the PV

τ = PM-tube resolving time (i.e., average length of time to pass through the PV).

It can be seen from Equation (3.1) that the probability of one or more scatterers being simultaneously in the PV (in other words, the probability of interference) is given by

$$P_{int} = 1 - P(o,x). \tag{3.2}$$

Analyses to estimate P_{int} have been done with varying degrees of depth by several authors [7,8,9,10,11]. In most cases, P_{int} was set at some specified value acceptable to the experimenter and was then related to other experimental parameters. The final formula involved a choice between specifying either the size of the control volume, or the maximum total concentration to be measured.

The most rigorous treatment was considered to be that done by Holve and Self [10]. Their analysis began with the Poisson probability

distribution in the manner of Equations (3.1) and (3.2), and then proceeded in terms of important experimental quantities such as the size range able to be measured and the total nuclei concentration, as well as an estimate of the overall size concentration distribution. The resulting formula for estimating coincidence errors was

$$P_{int} = \frac{n_T V_m}{(q-1)} \cdot \frac{1}{\log(d_{max}/d_{min})} \tag{3.3}$$

where P_{int} = acceptable probability of coincidence

V_m = probe volume size

d_{max}/d_{min} = ratio of largest to smallest size in the range that the PHA is set up to measure

n_T = total nuclei concentration

q = size concentration distribution parameter.

The variable q in Equation (3.3) comes from the assumption that the form of the size concentration distribution can be estimated as

$$N(d) = Ad^{-q}, \tag{3.4}$$

where d is the scatterer size, A is a constant, and q is always positive.

Due to its rigorous derivation, Equation (3.3) can be viewed as the general form of the error estimation formula, of which the estimation criterion of other investigators are special cases. For instance, in Reference [11] Keller's formula for estimating coincidence errors is

$$P_{int} = \frac{n_T V_m}{2} . \tag{3.5}$$

In both References [7] and [8], the conclusion is that the PV size which minimizes coincidence errors is given by

$$1 = n_T V_m \ . \tag{3.6}$$

In the present investigation, Equation (3.3) was used to estimate coincidence errors, and the experimental conditions involved resulted in the following formula:

$$P_{int} = \frac{n_T V_m}{1.43} \ . \tag{3.7}$$

The actual conditions which gave rise to Equation (3.7), together with an analysis of the resulting experimental data, are given in Section 5.1.

3.1.3 Illumination Error Criterion. In treating the inaccuracies associated with improper scatterer illumination, one must deal with the problem of non-uniformity in the laser beam intensity distribution itself. In Appendix A of Reference [11], Keller attempts such a treatment by postulating regions of uncertainty surrounding the control volume. The assumption is made that the ratio of the incorrect measurements (due to illumination errors) to the total number of measurements is equal to the ratio of this uncertainty area to the total area of the PV, normal to the flow. This model of the PV and the resulting error estimation formula are given in Figure 4.

However, this model assumes a uniform laser light intensity in the region of the PV which is not part of the uncertainty region, an assumption which Keller himself shows does not represent physical reality [11]. In fact, the laser beam has a Gaussian intensity

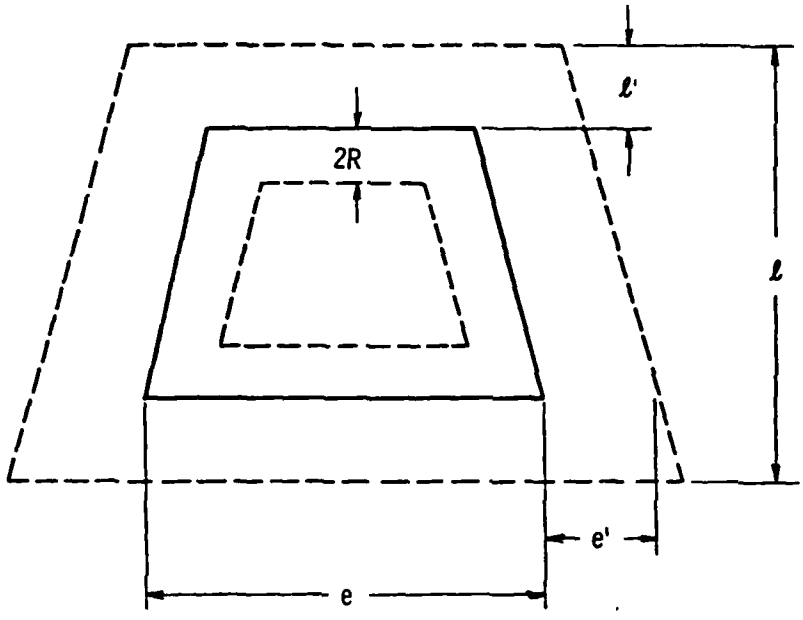

$$f\,(\%) \;=\; 100\left\{\ell - \frac{(\ell-2\ell'-4R)\,(e-2e'-4R)}{\ell e}\right\}$$

Figure 4. Keller Model of the Probe Volume and Illumination Error.

distribution, and this occurs only under ideal experimental conditions. It was also observed in this investigation that the Probe Volume illumination intensity could not be assumed to be uniform, or even Gaussian. Therefore, it was concluded that a fundamentally different analysis must be used to estimate the effect of illumination errors, one which would take into account the non-uniformity of the laser beam. Such an analysis is detailed in Section 3.3.

3.2 The Modified Measuring Subsystem

3.2.1 Principle of the Dual-Detector Operation. As mentioned previously in the system description, the inability of the LSS to distinguish between microbubble nuclei and solid particulate nuclei is due to an under-utilization of the full Mie-scattering properties of the nuclei. The potential for this distinguishability comes through the solution to the transverse angular solution of the full Mie scattering equations (see Equation (A.4)). This solution has the form

$$\Theta(\theta) = P_n^{(m)}(\cos\theta), \tag{3.8}$$

where $P_n^{(m)}$ are the Legendre polyromials. The fact that the argument of the Legendre polynomials is $\cos\theta$ indicates that the solution is symmetric at about $\theta = 0$. Therefore, the intensity of scattered light at $\theta = 90^o$ will be the same as at $\theta = -90^o$, but only if the nuclei are ideal Mie scatterers, that is, spherically symmetric.

This property of the scattering equations allows one to take advantage of the difference in geometry between microbubble and solid particulates. The microbubbles, being spherical, will cause symmetric

light-scattering, whereas the particles are in general randomly shaped and, therefore, will scatter light randomly. In principle, the way to separate measurements of bubbles from measurements of solid particulate is to compare the scattered light intensity from both $\theta = 90^{o}$ and $\theta = -90^{o}$. In practice, the issue is the establishing of a criterion for the cutoff asymmetry of scattering: That is, how equal must the scattered intensities at these two locations be in order for the scatterers to be considered as microbubbles; or similarly, how unequal must they be in order to be considered as solid particulates?

3.2.2 A Theory for Scattering by Non-Symmetric Particles. This question has been addressed in a recent analysis by Kohler and Billet [12] where the asymmetry ratio of a general randomly-shaped particle is calculated as a function of its orientation (with respect to the incident beam axis), and as a function of its axial ratio and refractive index. The asymmetry ratio, R, is defined as the ratio of the smaller magnitude scattered intensity to the larger. The axial ratio is defined as the ratio of the particles semi-minor axis to its major axis, and comes from considering the general randomly-shaped particle to be an ellipsoid or revolution or a prolate spheroid.

In this analysis, scattering calculations were made for many positions within the solid angle subtended by the receiving optics. These calculations were performed for a number of different particle orientations to describe the scattering in both directions ($\theta = \pm 90^{o}$) as functions of orientation angles, then the ratios of these scattered intensities resulted in R. Integrating R over all possible orientations of the random particle gave an average intensity ratio, $\bar{R}$.

This same integration procedure was used to compute the standard deviation (SD) from the average intensity ratio. In analyzing the characteristics of $\overline{R}$, they showed that it is nearly independent of both the particle size and refractive index. The critical factor was the axial ratio of the particle. Thus, the values of $\overline{R}$ and SD computed at one axial ratio would be general for all sizes and refractive indices.

Choosing an axial ratio of 1.76, Kohler and Billet computed an $\overline{R}$ of 0.45 and a SD of 0.33. Assuming that the random orientations were distributed normally, the normal distribution then predicted that 84% of the orientations would have a value of R less than $\overline{R}$ + SD. After adjusting the value of SD to account for computational errors, this R value was given as $\overline{R}$ + SD = 0.75, and was taken to be the cutoff asymmetry ratio, R_c.

This analysis thus provided the theoretical basis for separating measurements of microbubbles and measurements of solid particulate in a laser light-scattering system.

3.2.3 Method of Dual-Detector Operation. The schematic diagram for a modified LSS which has this microbubble distinguishing capability is shown in Figure 5. The difference from the original system shown in Figure 3 is that now there are two photo-detecting devices, one at $\theta = 90^{\circ}$ and the other at $\theta = -90^{\circ}$. Each has its own set of receiving optics and its own signal conditioner, and the output of these signal conditioners then go into a new electronic device called the Pulse-Height Comparator (PHC). The PHC performs the comparison of the

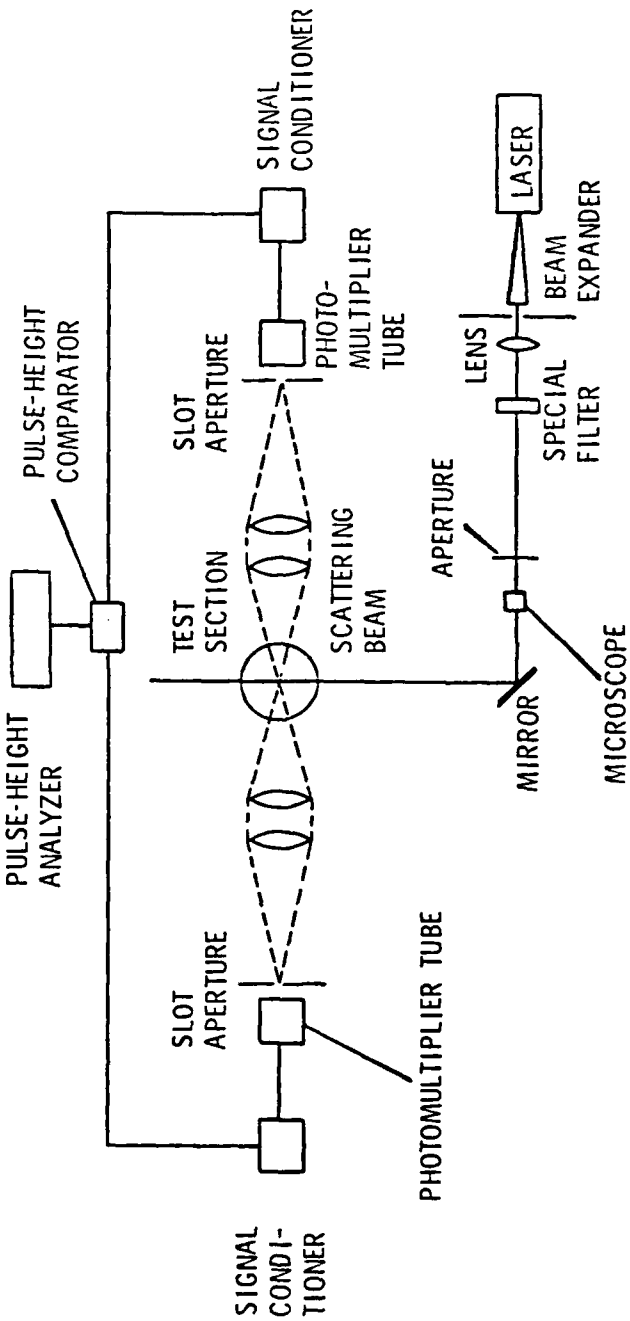

Figure 5. Schematic Diagram of the ARL/PSU LSS.

scattered intensities (now in the form of electronic signals) described in the previous analysis. If the compared signals give a value of R which is less than R_c, then the signals are rejected and no further signal processing occurs. If the compared signals' intensity ratio is greater than or equal to R_c, then the signals are passed on to the PHA to be sorted into the appropriate size channels.

In this investigation, experiments were conducted to test the validity of the cutoff asymmetry ratio, R_c, predicted by Kohler and Billet, and in so doing prove the effectiveness of the dual-detector system as a means of distinguishing microbubbles and solid particulate cavitation nuclei. The results of these experiments are given in Section 5.2.

3.2.4 Some Implications of This Method for Solving Control Volume Inaccuracies. An important additional effect of the dual-detector scattered light comparison method relates to the problem of illumination errors described in Section 3.1. It was mentioned that one cause of this kind of error was large nuclei (i.e., nuclei whose size is of the same order of magnitude as the CV) passing through an "edge" of the control volume so that only part is illuminated. This situation is a departure from an ideal Mie scatterer because in order for nuclei to scatter light symmetrically they must be illuminated by a uniform plane wave. Therefore, because the nucleus is non-uniformly illuminated, it will scatter light asymmetrically, and thus be rejected as a solid particle nucleus by the PHC.

So, in addition to providing a nuclei-distinguishing capability to the LSS, the dual-detector system also eliminates the need for an

analysis to account for illumination errors caused by nuclei crossing an edge of the PV.

3.3 The Modified Analyzing Subsystem

3.3.1 Principle of the Nuclei Counter Inaccuracy. Another major problem observed in the LSS was the inaccurate classification of nuclei according to size and concentration, as reported by the Pulse-Height Analyzer (PHA). This inaccuracy is demonstrated clearly in Figures 6a and 6b, which show the size distribution from a typical nuclei measurement experiment as given by the methods of laser light-scattering and holography. The problem does not lie with the Mie theory calibration relationship itself, nor does the problem appear to be caused by the geometry of the optics used, since the same problem was documented by researchers using a near-forward scattering system [10]. These same researchers concluded that the problem was caused by a non-uniform intensity in the volume of laser light used to measure the nuclei (i.e., the PV).

As mentioned in Section 3.1, such non-uniformity in the PV illumination intensity was clearly observed in this investigation. Figures 12a and 12b show a survey of the illuminating laser beam (using a 30 μm aperture attached to a photodetector) made before the beam enters the water tunnel test section, and then another survey of the beam inside the test section. The obvious conclusion to be drawn is that the intensity in the PV cannot be assumed to be uniform, even if the incident beam is made uniform.

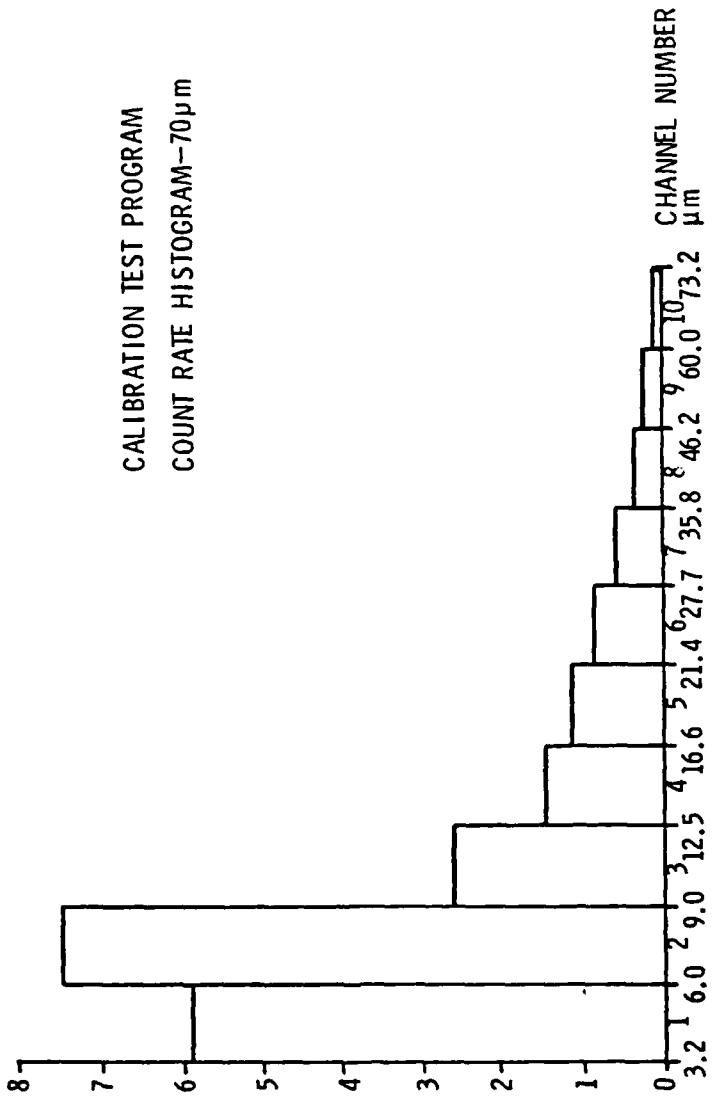

Figure 6a. Count Rate Distribution Given by the LSS for the 70-µm Experiment.

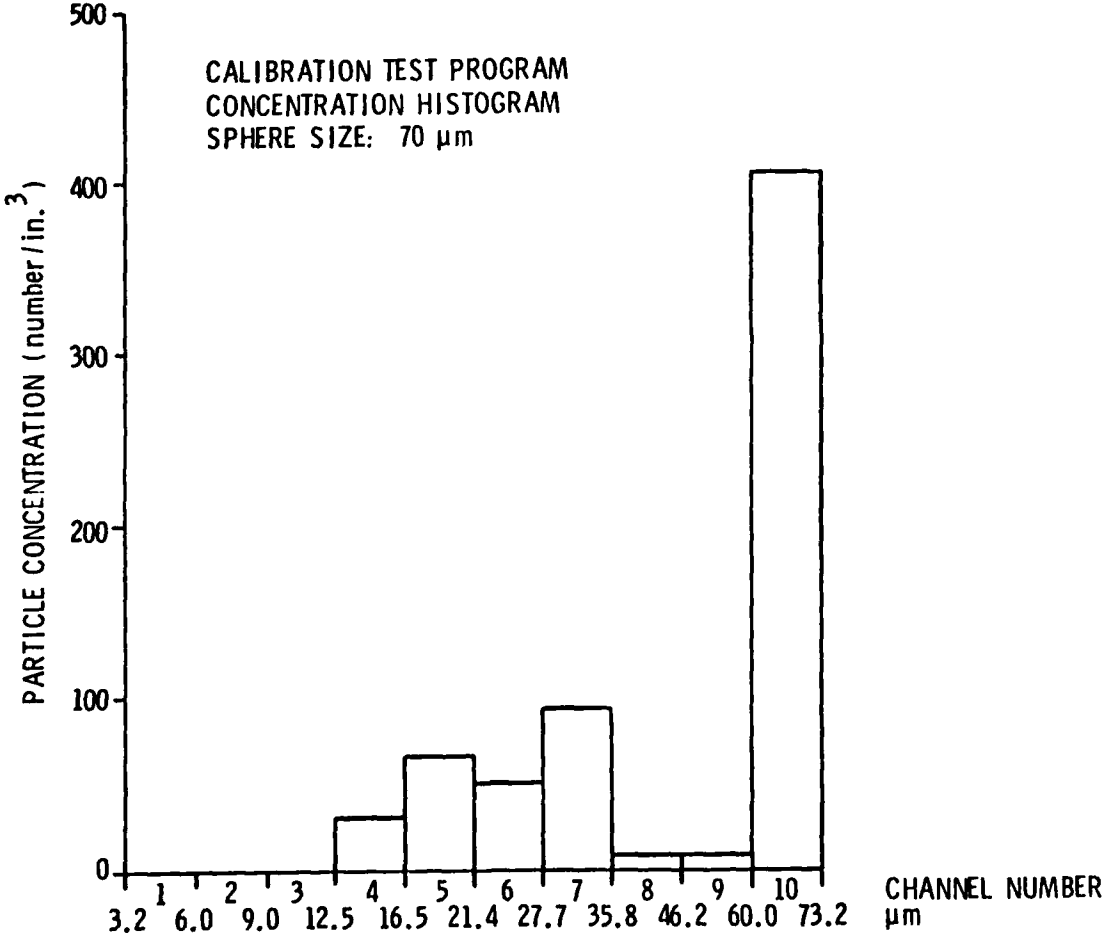

Figure 6b. Nuclei Concentration Distribution Given by Holography for the 70-µm Experiment.

3.3.2 Method of Matrix Inversion. To deal with the non-uniform intensity problem, the researchers in Reference [10] developed a mathematical method to correct the count rate data given by their particle counter. The method is called an inversion scheme, and the technique used to deal with inaccuracies in the nuclei counter (i.e., PHA) was patterned after this method. The basis of the technique is to consider that the governing Mie scattering equation has a variable incident beam intensity instead of a constant one (see Equation (B.1)). The effect is that the equation used to convert count rate data into concentration data is changed in the following way. The actual data histogram given by the PHA is in terms of count rate, that is, the number of nuclei counted per unit time. The physically relevant quantity is the nuclei concentration. These quantities were considered to be related by a constant as

$$C_i = USN_i, \tag{3.9}$$

where C_i = count rate of nuclei in channel i, as reported by the PHA

U = speed of nuclei through the control volume

S = area of the control volume normal to the flow direction

N_i = concentration of nuclei of size category i.

The effect of a variable incident beam intensity on Equation (3.9) is to change it to a matrix equation expressed as

$$C_i = US_{ij}N_j, \tag{3.10}$$

where S_{ij} = matrix of area elements which transforms the vector of concentration data into the vector of count rate data.

In order to have a method of transforming count rate data into concentration data, which is what is needed for the nuclei counter, Equation (3.10) is solved for N_j, yielding

$$N_j = \frac{1}{U} S_{ij}^{-1} C_i. \tag{3.11}$$

Physically, Equation (3.11) states that the nuclei concentration of a given size category is not merely the corresponding count rate from that category, but is actually a weighted sum of the count rates from all channels in the nuclei counter, where the weighting factors are the inverted elements of the area matrix, S_{ij}. The variation of the elements in this matrix reflects the variation of the illuminating beam intensity in the PV; therefore, the matrix should be constant for a given laser and optical arrangement, so that theoretically the elements need only be calculated once for a given arrangement. This also implies that this classification inaccuracy phenomenon should be seen more clearly as the number of nuclei measured by the system becomes statistically large, since in time these nuclei will sample all regions of the PV and thus experience the full extent of its non-uniformities. A more detailed summary of the inversion scheme developed by Holve and Self [10] that formed the basis for this analysis is given in Appendix B.

In this investigation, a series of calibration experiments were carried out where U, C_i, and N_i were measured under many different conditions in order to solve for the elements of the area matrix, S_{ij}, so that this matrix could be used according to Equation (3.11) to correct the count rate histograms obtained with the light-scattering system.

CHAPTER 4

EXPERIMENTS TO TEST PROPOSED SOLUTIONS

4.1 Experiments Involving Nuclei Distributions

4.1.1 Experimental Objectives and Methods. The objectives of this series of experiments were to determine the cutoff level for the Pulse-Height Analyzer (PHA) for the separation of microbubble and solid particulate nuclei and to determine the elements of the area matrix, S_{ij}. The definition of S_{ij} is the key to the operation of the inversion scheme for correcting some inaccuracies.

The operating parameter of the Pulse-Height Comparator (PHC) is the cutoff rejection ratio, R_c, defined in Section 3.2.2. Defining this parameter requires not only an estimate of the scattering characteristics of non-symmetric particles, but also an estimate of the asymmetry of sphere scattering under actual test conditions. The method used to obtain those estimates was to program a variable cutoff rejection ratio in the PHC. Estimates of sphere-scattering asymmetry were then obtained by measuring the number of spheres rejected as a function of R_c for several different sphere size monodispersions. Similarly, estimates of non-symmetric particle scattering were obtained by measuring the total number of rejected scatterers (both spheres and particles) for a mixture of microspheres and non-symmetric particles.

In order to determine the elements of the area matrix, S_{ij}, measurements of count rate, C_i, and concentration, N_j, were made of single-size concentrations (or monodispersions) of spheres. The goal was to measure monodispersions representing each of the 10 size

categories in the nuclei classification system. Such a set of measurements would allow the elements of S_{ij} to be solved for each of the 10 columns in the matrix. The form of this matrix would then be 10 by 10, and would be upper-triangular (i.e., all elements below the main diagonal are zero). The upper-triangular form is a result of the fact that a given scatterer will not appear larger than its Mie-predicted size, since this predicted size is based on the scatterer passing through the peak intensity portion of the PV. Appendix B gives a more complete derivation of the equations governing this experimental procedure.

4.1.2 Description of Equipment. Figure 7 gives a simplified schematic diagram of the overall experimental set-up used. This set-up has three independent subsystems:

1. Korad Holography System (KHS) - The holography system was used to calibrate the light-scattering system (LSS). As the LSS was measuring the concentration of a given size category, a hologram of a representative volume of the flow during the period of the LSS measurements was obtained. Reconstruction of a magnified image of the hologram allowed the scatterers to be actually visualized, sized and counted to give the concentration measurements, N_j. Figure 8 shows a schematic diagram of the equipment used to reconstruct the holograms and measure the nuclei concentrations.
2. Water Tunnel and Pressuring System - This system provided the means for controlling the nuclei population in the

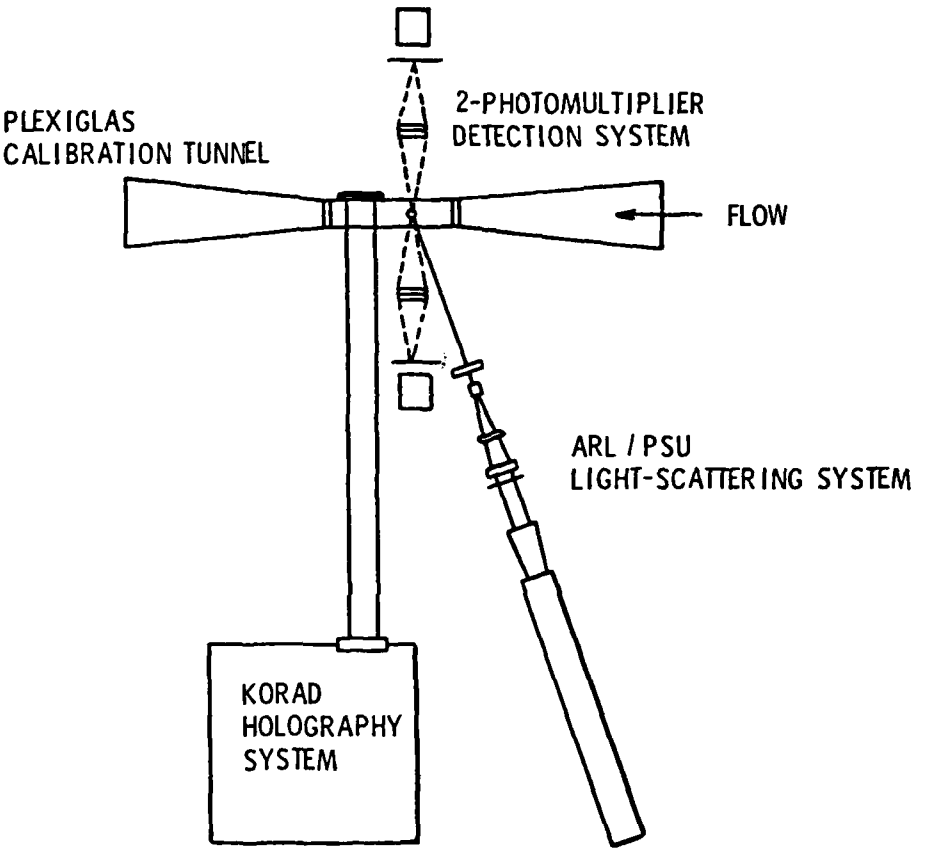

Figure 7. Simplified Schematic of Experimental System.

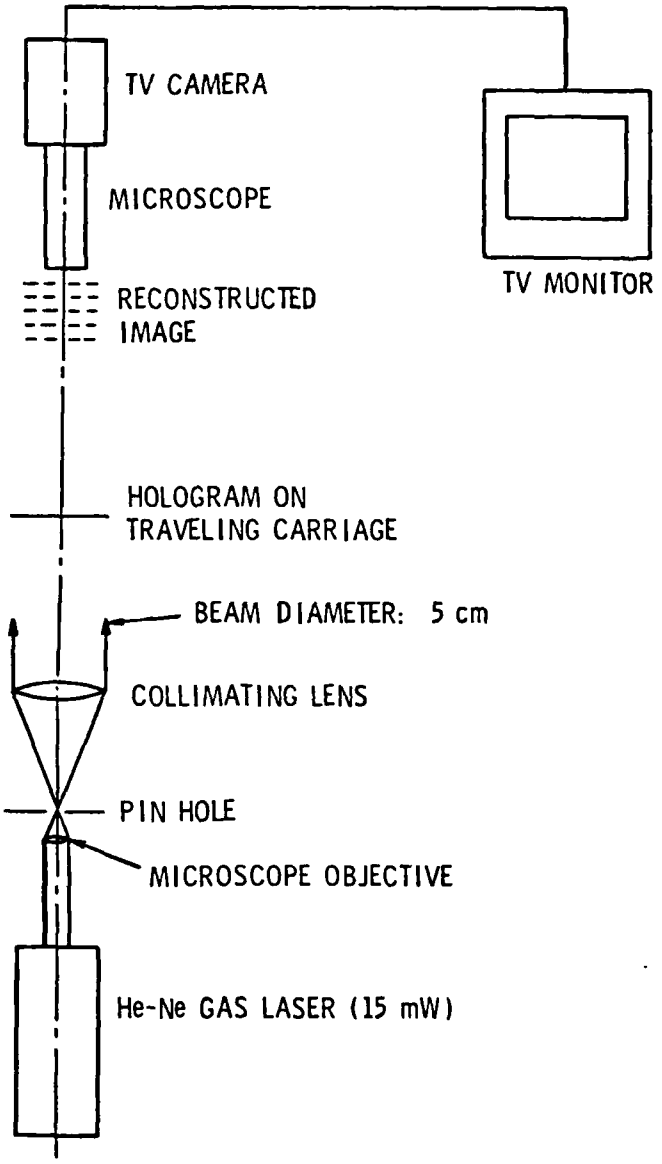

Figure 8. Schematic of the Hologram Reconstruction System.

experiments and is shown in Figure 9. The water tunnel itself was designed and built especially for this investigation. It was constructed of plexiglas with a fiberglas casing and had a 3-inch by 3-inch square cross-section, except for the test section which was 1 inch by 3 inches and 6 inches in length. Power was provided by a 2 hp centrifugal pump, made of cast iron and treated with an epoxy sealant to inhibit rust formation. The pump motor was rated at 3425 rpm, but a frequency inverter was connected to the motor to obtain speed variation.

Purity of the water sample used in experiments was achieved in the following way. Distilled water (with a filtration purity of 2 μm) was used as the water sample and was contained in a 30-gallon sealed drum. A rust inhibitor (nickel chromate) was added to suppress the formation of rust in the pump machinery and, therefore, minimize the contribution of rust particles to the background nuclei concentration. The water in this container was then subjected to a vacuum of approximately 5 psia for a period of between 12 and 36 hours to remove as much of the air dissolved in the sample as possible. During the operation of the experiment, the water tunnel was pressurized to a maximum of 8 psia in order to suppress the generation of bubbles from cavitation in the pump machinery.

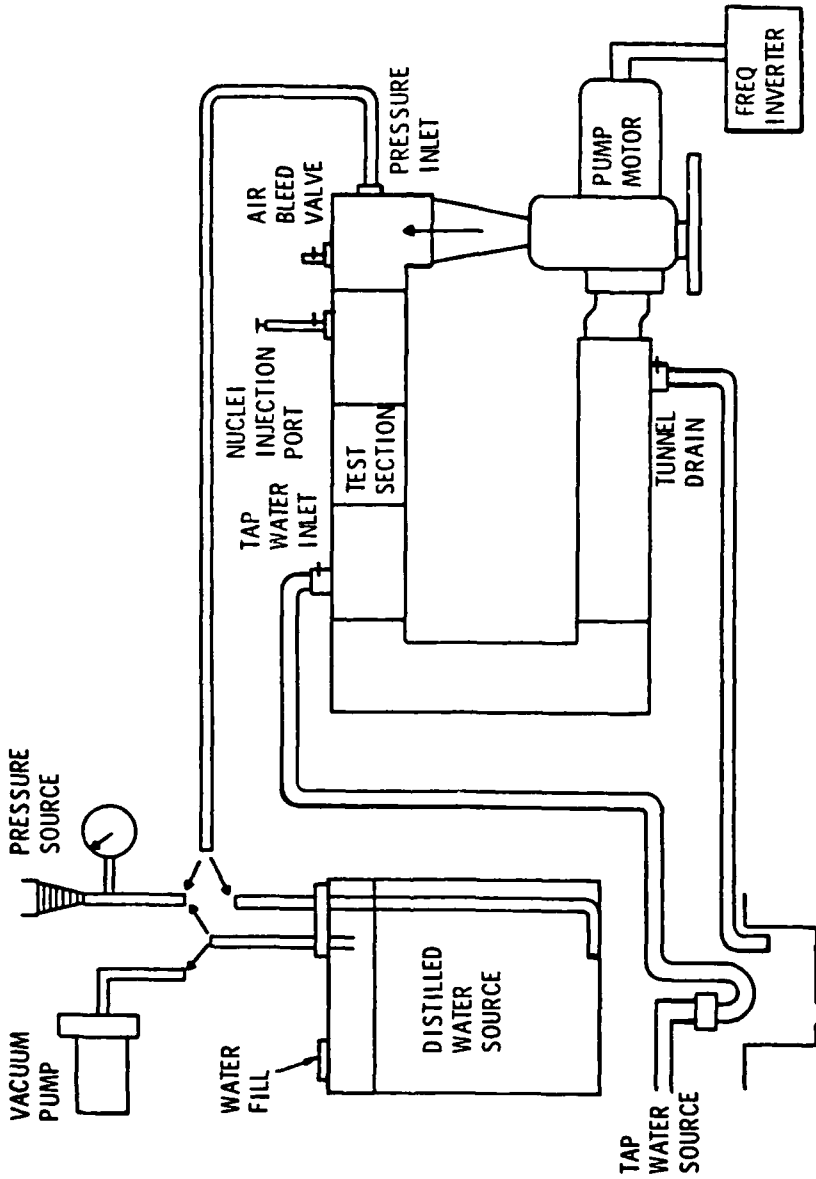

Figure 9. Schematic of the Water Tunnel and Pressuring System.

3. Light-Scattering System (LSS) - The LSS used in the experiments was different from that detailed in Chapter 2 only in that both the old and new PHA's were used. The old PHA, which interpreted data from only one PM-tube, was used to calibrate the new, two-PM-tube PHA; that is, the old PHA was used to make sure that the two PM-tubes, which feed into the new PHA, had equal amounts of amplifier gain. This was important to assure that both PM's were indeed measuring the same signals before comparisons of differing signals in the PHC could be made with confidence. The matching procedure was to feed the output of each detector into an older model nuclei classification system, which was based on only one output. The counting times of each detector would be noted as they measured an actual steady flow; then the electronic gain on the amplifiers associated with the detectors would be adjusted until both detectors would consistently give the same counting rate. One detector was the one with which the calibration relationship between nuclei size and detector voltage was determined, then the second detector's amplifier gain was matched to this one. Figure 10 shows a schematic diagram of the equipment used in the experimental version of the LSS.

4.1.3 Procedure for the Experiments. The following is the chronological procedure used in the experiments at the Materials Research Laboratory of The Pennsylvania State University.

4.1.3.1 Initial preparations.

1. Calibration particles - In order to control the nuclei concentrations in the experiments, it was necessary to use scientific calibration particles. To model the cavitation bubble nuclei, latex microspheres [13] were used. These came in the form of a suspension, with approximately 10^6 spheres to a 10-mℓ bottle if the sphere size was greater than 24 microns (μm) in diameter. The number was 10^7 if the sphere size was less than or equal to 24 μm. To model the non-symmetric solid particulate nuclei, a calibrated dust particle sample was used which had a size range of 20 to 25 microns in mean diameter guaranteed by analysis [14].
2. PHA calibration curve - The objective here was to put the scattered light intensity relationship depicted in Figure 1 in terms of actual PM-tube voltage. This was done by using an alternate test section in the water tunnel, one which had an open top. The tunnel was subsequently filled with water, and latex spheres of a known size were then manually injected into the laser PV while their corresponding voltages were recorded on an oscilloscope. Only a few sizes needed to be tested in this way to establish the entire voltage calibration curve.

3. PHA classification channels - After the voltage calibration curve was obtained, it was then necessary to determine the size and number of nuclei classification channels in the PHA that were appropriate to the experimental conditions. An attempt was made to measure an order of magnitude of sizes from 5 to 70 microns, and this range was spanned with 10 classification channels so as to reduce the amount of experimentation necessary. The relative widths of the channels were scaled logarithmically; that is, the upper limit voltage amplitude, A_i, of a given channel i was related to the upper limit voltage amplitude of the next channel, A_{i+1}, according to

$$\frac{A_{i+1} - A_i}{A_i} = \beta, \qquad (4.1)$$

where β is an arbitrary constant.

4. Matching of photo-multiplier output - The matching procedure used in the experiment followed the procedure described in Section 4.1.2. Typically, as seen in Figure 10, the detector labeled PM 1 was the one used to establish the voltage calibration curve, and then detector PM 2 would have its amplifier gain adjusted until its counting time was matched to PM 1.

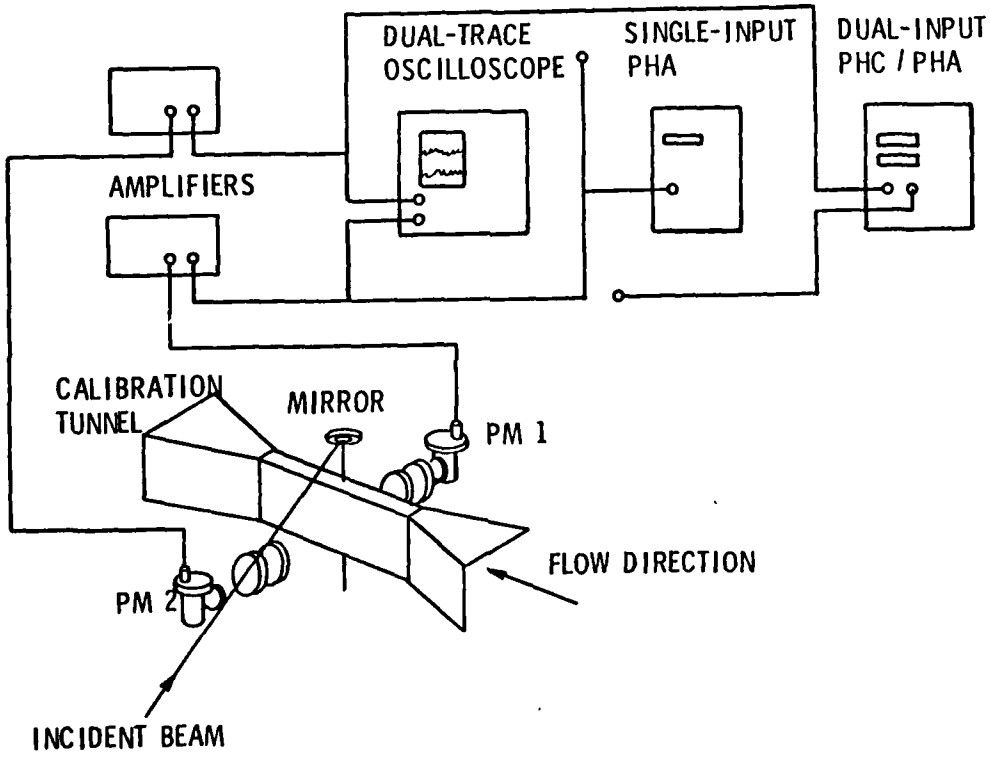

Figure 10. Schematic of the LSS Equipment Used in Experiments to Measure Nuclei Distributions.

4.1.3.2 Typical nuclei test procedure.

1. Tunnel cleaning and preparation - The tap water source was connected and the empty tunnel was allowed to fill (refer to Figure 9). When full, the drain was opened and the pump was turned on at a low speed, with the tap water still running. The tunnel was flushed out like this for about 20 minutes, and then drained.

   Next, the pressure line was connected to the distilled water. When the tunnel was full, the pump was turned on and the water was allowed to run through the tunnel for about 20 minutes. After this water was drained, the tunnel was refilled with a fresh sample of distilled water.

2. Background measurements - The system's laser (spectra-Physics 4-watt, argon-ion) was turned on and focused into the test section. The laser's blue line (4480 angstroms) was used, and the power was set at 500 mW. The pump was turned on and brought up to a flow of 12 feet per second at the test section, which corresponds to 2000 rpm at the motor. The background noise level remaining in the tunnel after cleaning was then used as the steady count rate in rechecking the matching of the photo-multiplier signals.

When rechecked, both PM were connected to the dual-input combination PHC/PHA (refer to Figure 10) and the background count rate was measured 10 consecutive times. This was done without comparison of signals in the PHC, which is an effective cutoff rejection ratio of $R_c = 0.0$.

3. Nuclei distribution measurements - While the tunnel was still in operation, the size concentration to be measured was introduced into the tunnel through the nuclei injection port (Figure 9). Generally, one entire bottle of calibration spheres would be introduced into the tunnel for a given test. After the spheres had been injected, the PHC/PHA was used to take 10 consecutive measurements of the nuclei count rate with no comparison in the PHC.
4. Begin discrimination effectiveness data - Without stopping the tunnel, the PHC was switched to the discriminating mode, with R_c set at 0.50, and the series of 10 nuclei counts was taken. This procedure was repeated for $R_c = 0.60$.
5. Holography measurements - While the above measurements were being taken, the KHS was prepared for use. After the last nuclei count was made with $R_c = 0.60$, the tunnel pump was turned off, and two or three holograms were

immediately taken. Shutting off the pump was found to be necessary in order to eliminate vibrations that blurred the hologram image. Then it was necessary to wait approximately one half hour for the holograms to be developed before proceeding with the test.

6. Continue discrimination effectiveness data - After the holograms were developed, the tunnel was restarted, and several measurements of the count rate, using no comparison in the PHC, were made as a recheck. Then, the procedure begun in Step 4 was resumed, with cutoff rejection ratios of 0.70, 0.80, and finally 0.90 being used in the PHC.
7. Test completion - When the measurement of the discrimination effectiveness data was completed, the pressure line was removed from the distilled water source and connected directly to the water tunnel inlet, and the tunnel was then drained under pressure.

4.1.3.3 Scope of the nuclei tests. The typical nuclei test was followed for a number of different nuclei distributions. To calibrate the area matrix, S_{ij}, the original intention was to measure calibration sphere monodispersions representing each size category in the PHA. The representative monodispersons were chosen to be the following: 5 μm, 7 μm, 10 μm, 15.5 μm, 19 μm, 24 μm, 31.2 μm, 40 μm,

50 μm, and 70 μm, representing channels 1 to 10, respectively. However, during the process of conducting the experiments, it was found that the holography system had a resolution limit of 15 μm; thus, the data from the 5-μm, 7-μm, and 10-μm tests could not be interpreted.

Two mixtures of calibration spheres were measured using this typical test procedure, each composed of three different sphere sizes. Sphere mixture I was made up of one bottle each of 49.3-μm, 31.2-μm, and 15.5-μm spheres; sphere mixture II was composed of one bottle each of 50-μm, 24-μm, and 15.5-μm spheres. The holograms, taken in conjunction with sphere mixture I, could not be interpreted, so only the data from mixture II was usable.

Finally, a mixture of both spheres and calibrated dust particles was measured. The sphere size used was 70 μm, and the dust was the 20 to 25 μm mean diameter particles described earlier.

4.1.3.4 Hologram reconstruction. As mentioned in Section 4.1.2, independent measurements of the concentrations were made possible through the KHS. As can be seen in Figure 8, such measurements were obtained through viewing a reconstructed and magnified image of the hologram. The magnification of the system was set by the microscope objectives, a value of 200x for this investigation.

As the hologram was moved along the axis of the reconstruction system, different planes of the three-dimensional image would come into focus. At each such focus, the carriage could be moved horizontally or vertically to allow nuclei to be counted. Using three directions

of motion, the number of spheres in an arbitrary volume could be counted and so calculate a local concentration.

This concentration was then adjusted by a correction factor that accounted for frequency-shifting of the holography laser beam in water. This correction factor was calculated by Vikram [15] to be

$$V_{actual} = (1.12)\ V_{measured}. \tag{4.2}$$

4.2 Experiments Involving Laser Intensity Distributions

4.2.1 Objectives of Experiments. After the experiments involving laser sphere distributions were completed, analysis of the data revealed that the elements of the area matrix (S_{ij}) calculated from these data did not satisfy all the criteria that would prove the validity of the inversion scheme. A possible cause of this was a temporal as well as spatial variation of the laser intensity distribution at the PV. The effect of this would be that each individual test had the potential of experiencing a different matrix of area elements, even though the optical arrangement was the same for each test.

Experimental measurements of the laser intensity distribution were obtained so as to accomplish three goals: First, to document spatial and temporal variations in the laser intensity; second, to find ways to minimize these variations; and third, to isolate the contribution of laser intensity non-uniformities to the overall inaccuracy of the count rate data.

4.2.2 Description of Experiments

4.2.2.1 Documenting intensity variations. As shown in Figure 11, the intensity profile was measured at two different locations

along the laser beam's path. Position 1 was 2 to 3 feet from the laser course and about 6 inches in front of the pinhole aperture. Position 2 was approximately 6 feet from the laser source. This position was supposed to be a model of the actual condition of the PV in ARL's 12-inch diameter water tunnel; thus, Position 2 was located at a point where the beam had passed through a 1-inch thick plexiglas window and then through 6 inches of water.

Measurements of the intensity profile were obtained through the use of a photo-detector mounted on a movable carriage. The photo-detector was marked with a 30-μm diameter pinhole aperture, and the carriage allowed this aperture to be moved horizontally and vertically in fixed increments so that the entire cross-sectional area of the beam could be scanned.

In addition, the mirror in Figure 11a could be removed so that the beam could be examined on a screen at a distance of approximately 10 feet from the laser source. The intensity profile was not scanned with the photo-detector at this distance. Instead a lens was used to magnify the beam so that its cross-section could be inspected visually on the screen.

4.2.2.2 Minimizing variations. When the mirror was removed and the beam intensity was inspected visually, it was observed that the beam became seriously distorted within 18 inches after passing through the second lens. Therefore, several different lenses were used, and the position of the lens with respect to the beam was varied in order to improve the intensity distribution.

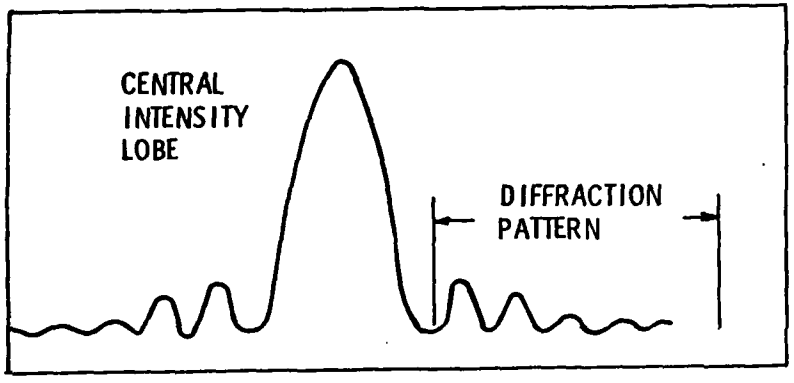

Figure 11b. Model of Laser Intensity Distribution in the Probe Volume Due to Diffraction Pattern.

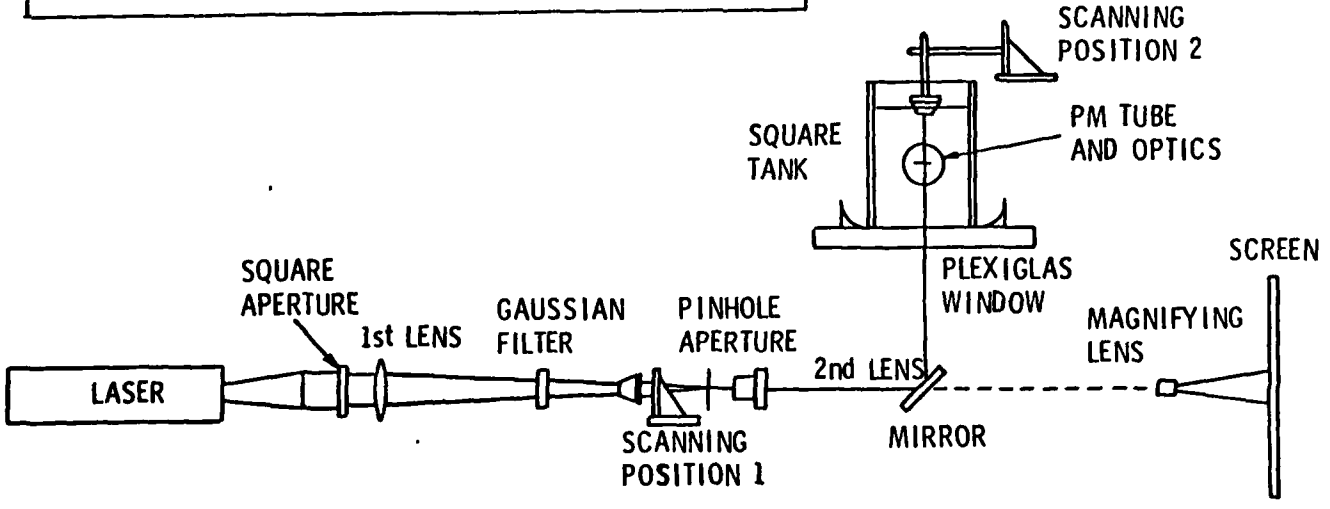

Figure 11a. Schematic of the Equipment Used in Experiments to Measure Laser Intensity Distributions.

The beam was observed to have a diffraction pattern around its cross-section which was rectangular in shape like the laser beam itself. To eliminate this, several different sizes of pinhole apertures were tried. These varied from 25 μm in diameter to 400 μm. In addition, a series of rectangular apertures were made in order to find one which would most closely match the size and shape of the beam's central intensity lobe (see Figure 11b).

4.2.2.3 Contribution of non-uniform beam to count rate inaccuracy. It was decided that the way to isolate the contribution of the PV intensity profile to the inaccuracy of the count rate distribution given by the PHA was to obtain measurements of a monodispersion similar to the tests described in Section 4.1.3, except that the beam intensity profile would be measured at the time of the experiment.

This experiment was carried out using 70-μm spheres in the square tank shown in Figure 11a. The water in the tank was stirred to give the spheres a velocity through the control volume. Prior to the measuring of the sphere count rate, the intensity profile was measured in both Positions 1 and 2. The measurement at Position 2 was made immediately prior to measurement of the count rate.

In Appendix C, an analysis is performed which generates data allowing a comparison to be made between the count rate distribution obtained from this experiment and the distribution that should have resulted according to these measurements of the intensity profile.

CHAPTER 5

PRESENTATION OF DATA

5.1 Probe Volume Error Analysis

5.1.1 Experimental Conditions. In Chapter 3, the formula used to estimate errors was given as

$$P_{int} = \frac{N_T V_m}{(q-1)} \cdot \left[\log\left(\frac{d_{max}}{d_{min}}\right)\right]^{-1}, \tag{3.3}$$

which under the conditions of this experiment gave rise to a coincidence error criterion of

$$P_{int} = \frac{N_T V_m}{1.43} . \tag{3.7}$$

The coefficient in Equation (3.7) is the combination of the size range parameter, d_{max}/d_{min}, and the size concentration distribution parameter, q. The size range programmed into the PHA was 5 μm to 70 μm, giving a size range parameter of 14. The value of q was obtained from a composite plot of bubble nuclei concentration measurements compiled by Gates [16]. A linear regression of the data on his log-log plot yields a functional relationship approximated as

$$N(r) = A_r^{-2.25} . \tag{5.1}$$

Thus, q was taken to be equal to 2.25, and when substituted into Equation (3.3) gave the relation in Equation (3.7).

The lens system that the laser beam passed through produced a width of 0.67 mm observed at the Probe Volume. This, together with a slot aperture width of 0.025 inches placed over the PM-tubes, gave a PV size of $2.85 \times 10^{-4} cm^3$.

5.1.2 Analysis of Coincidence Errors. Given the size of the PV used in the experiments, Equation (3.7) allows the probability of coincidence to be estimated if the total nuclei concentration, N_T, is known. Table 1 shows the relationship between the nuclei concentration and coincidence probability for several of the experiments involving nuclei distributions. The measurements of concentration were obtained by using the holography system.

It can be seen that the tests involving the 40-μm, 50-μm, and 70-μm spheres, as well as the 70-μm spheres and dust mixture, all had quite low coincidence errors. The 15.5-μm, 19-μm, and sphere mixture II tests all had very high coincidence errors, with more than one out of every three events being a coincidence.

5.2 Performance of the Dual-Detector System

5.2.1 Method of Proof. As detailed in Chapter 3, the proof of the dual-detector system's effectiveness would come through verifying the theory for non-symmetric particle scattering in actual practice. In addition, it would be necessary to gain an estimate of the asymmetry of scattering by spheres.

These proofs were obtained in the experiments by recording the responses of several calibration sphere monodispersions to different values of the cutoff asymmetry ratio (R_c) used in the system's Pulse-Height Comparator (PHC). In the same way, a mixture of calibration

TABLE 1

RELATIONSHIP BETWEEN NUCLEI CONCENTRATION AND COINCIDENCE ERROR

Nuclei Test	Total Concentration $N_T(in^{-3})$	Coincidence Probability P_{int}
70-μm spheres	407.7	0.005
50-μm spheres	835.7	0.010
40-μm spheres	3875	0.047
24-μm spheres	12510	0.152
19-μm spheres	30970	0.377
15.5-μm spheres	31310	0.381
70-μm spheres and dust particles	3933.3	0.048
sphere mixture II	23896	0.413
(50 μm, 24 μm, and 15.5 μm)		

spheres and calibrated dust particles was tested to verify the theory for non-symmetric particle scattering.

5.2.2 Analysis of Data. Table 3 gives the compiled results of all the experiments involving microsphere distributions and their responses to changes in the PHC cutoff rejection ratio. The information for verifying the theory for non-symmetric particle scattering is contained in the data from the 70-μm spheres and dust mixture test; however, this data must first undergo a transformation in order for it to be in terms of the same variables used in the theory.

In the analysis of Kohler and Billet [12], the amount of screening achieved by a given level of R_c was the ratio of the number of non-symmetric (or dust) particles rejected to the total number of dust particles encountered by the PHC. This ratio is referred to here as R_{dust}, and is defined as

$$R_{dust} = \frac{N_{dust\ rejected}}{N_{dust}} . \tag{5.2}$$

In this investigation, both spheres and dust particles were examined by the PHC, so that the rejection ratio given was actually a composite, defined as

$$R_{composite} = \frac{N_{spheres\ rejected} + N_{dust\ rejected}}{N_{spheres} + N_{dust}} . \tag{5.3}$$

In the tests involving only microspheres, the rejection ratio of the PHC was defined in yet another way as

TABLE 2

REJECTION OF NON-SYMMETRIC PARTICLES AS A FUNCTION OF CUTOFF REJECTION RATIO (R_c)

Cutoff Asymmetry Ratio in PHC (R_c)	Sphere Rejection Ratio (R_{sphere})	Composite Rejection Ratio ($R_{composite}$)	Non-Symmetric Particle Rejection Ratio (R_{dust})
0.50	0.747	0.850	0.887
0.60	0.818	0.879	0.901
0.70	0.870	0.912	0.927
0.80	0.911	0.942	0.953
0.90	0.952	0.975	0.983

TABLE 3

SPHERE REJECTION DATA AS A FUNCTION OF R_c FOR ALL NUCLEI TESTS

Nuclei Test	Cutoff Asymmetry Ratio in PHC (R_c)	PHC Rejection Ratio
70-μm spheres	0.50	0.747
	0.60	0.818
	0.70	0.870
	0.80	0.911
	0.90	0.952
50-μm spheres	0.50	0.533
	0.60	0.638
	0.70	0.804
	0.80	0.912
	0.90	0.919
40-μm spheres	0.50	0.751
	0.60	0.895
	0.70	0.926
	0.80	0.957
	0.90	0.968
31.2-μm spheres	0.50	0.690
	0.60	0.766
	0.70	0.858
	0.80	0.936
	0.90	0.970
24-μm spheres	0.50	0.833
	0.60	0.897
	0.70	0.938
	0.80	0.969
	0.90	0.983
19-μm spheres	0.50	0.770
	0.60	0.917
	0.70	0.933
	0.80	0.962
	0.90	0.984
15.5-μm spheres	0.50	0.769
	0.60	0.821
	0.70	0.873
	0.80	0.921
	0.90	0.963

TABLE 3 (continued)

SPHERE REJECTION DATA AS A FUNCTION OF R_c FOR ALL NUCLEI TESTS

Nuclei Test	Cutoff Asymmetry Ratio in PHC (R_c)	PHC Rejection Ratio
10-μm spheres	0.50	0.796
	0.60	0.836
	0.70	0.887
	0.80	0.924
	0.90	0.968
70-μm spheres and dust particles	0.50	0.850
	0.60	0.879
	0.70	0.912
	0.80	0.947
	0.90	0.975
sphere mixture I (49.3 μm, 36.2 μm, and 15.5 μm)	0.50	0.818
	0.60	0.768
	0.70	0.925
	0.80	0.919
	0.90	0.960
sphere mixture II (50 μm, 24 μm, and 15.5 μm)	0.50	0.751
	0.60	0.885
	0.70	0.926
	0.80	0.957
	0.90	0.968

$$R_{spheres} = \frac{N_{spheres\ rejected}}{N_{spheres}}, \tag{5.4}$$

since in these tests there were no dust particles.

Equation (5.3) can be written in terms of the other rejection ratio as

$$R_{composite} = \frac{R_{spheres} + \frac{N_{dust\ rejected}}{N_{spheres}}}{1 + \frac{N_{dust}}{N_{spheres}}}, \tag{5.5}$$

or, substituting in Equation (5.2),

$$R_{composite} = \frac{R_{sphere} + (R_{dust} \cdot M)}{1 + M}, \tag{5.6}$$

where M is defined here to be the composition ratio of the mixture of spheres and dust particles,

$$M = \frac{N_{dust}}{N_{spheres}}. \tag{5.7}$$

Now, expressing the rejection ratio in terms of the quantities encountered in this investigation gives

$$R_{dust} = \left(\frac{1+M}{M}\right) R_{composite} - \left(\frac{1}{m}\right) R_{sphere}. \tag{5.8}$$

The composition ratio of the 70-μm sphere and dust particle mixture was calculated through the use of the concentration data obtained

from holograms during that test. According to the holography measurements, this ratio was

$$M = \frac{2903.8 \text{ dust/in}^3}{1029.5 \text{ spheres/in}^3} = 2.82 \ .$$

Using this value of M. Table 2 gives a comparison of the rejection ratio in Equation (5.8), as functions of the cutoff asymmetry ratio used in the PHC.

5.3 Performance of the Matrix Method

5.3.1 Correlations with Sphere Distributions

5.3.1.1 Criteria for proof of matrix method validity.

In providing the validity and usefulness of the matrix method as a means of correcting the cavitation nuclei size distribution data given by the light-scattering system's PHA, two proofs are required. First, there must be evidence that the matrix of elements, S_{ij}, representing the PV are intercepted by the nuclei, has an equi-diagonal character. That is, the experiments must give equality among elements of the same diagonal. The inversion scheme detailed in Reference [10] predicts that such a behavior will occur if two experimental conditions are met:

1. The channel widths in the PHA are scaled logarithmically (a condition detailed in Section 4.1.3).
2. The area function is independent of nuclei size (see Equation (B.2)).

Second, the matrix of elements, S_{ij}, obtained in experiments should successfully correct the PHA data from an experiment involving a random size distribution.

5.3.1.2 Comparison of results with proof criteria.

Table 4a shows the matrix of S_{ij} elements that were obtained through the experiments involving nuclei distributions. Each column of elements represents the results of one test, with the size measured listed at the head of each column. The diagonals are shown ordered as $S_1 \leq S_\ell \leq S_{10}$. Table 4b lists the average value of the elements in S_ℓ, denoted as $\bar{S}_\ell$, and the average deviation in each diagonal from the average value. From those two tables it can be seen that the equality of diagonal elements does appear, and that the range of spread in the deviation from each diagonal is also very similar.

With the area matrix exhibiting the characteristics predicted by the inversion scheme, this matrix was then used to correct PHA count rate data from two different random nuclei size distributions. One was the sphere mixture II, and the other was an actual cavitation bubble distribution measured in the 12-inch diameter water tunnel at ARL. In each case, the distribution data was corrected according to Equation (3.11) for three different matrices of elements. One was composed of the actual matrix elements obtained by experiments and is presented in Table 4a; the second was a matrix where all the elements along a diagonal were equal to the average diagonal value, as calculated in Table 4b; the third was similar in form to the second, except that the value along a diagonal was given by the 70-μm sphere test, shown as column 10 in Table 4a.

TABLE 4a

ELEMENTS OF THE AREA MATRIX (S_{ij}) CALCULATED FROM EXPERIMENTS

S_{ij}

Column Number

	4 15.5 μm	4 19 μm	6 24 μm	7 31.2 μm	8 40 μm	9 50 μm	10 70 μm
1	4.89×10^{-6}	2.35×10^{-6}	2.07×10^{-6}	4.65×10^{-6}	9.03×10^{-6}	1.41×10^{-4}	1.06×10^{-4}
2	4.79×10^{-6}	1.92×10^{-6}	1.14×10^{-6}	1.87×10^{-5}	1.78×10^{-5}	2.17×10^{-4}	1.33×10^{-4}
3	2.80×10^{-6}	1.10×10^{-6}	5.78×10^{-7}	2.43×10^{-5}	3.21×10^{-5}	7.32×10^{-5}	4.03×10^{-5}
4	1.77×10^{-6}	6.79×10^{-7}	3.98×10^{-7}	1.02×10^{-5}	2.45×10^{-5}	1.91×10^{-5}	2.50×10^{-5}
5		3.60×10^{-7}	2.47×10^{-7}	5.16×10^{-6}	8.37×10^{-6}	1.19×10^{-5}	1.97×10^{-5}
6			1.41×10^{-7}	3.16×10^{-6}	3.63×10^{-6}	7.83×10^{-6}	1.42×10^{-5}
7				1.70×10^{-6}	1.20×10^{-6}	4.77×10^{-6}	1.02×10^{-5}
8					8.46×10^{-7}	1.98×10^{-6}	5.84×10^{-6}
9						1.87×10^{-6}	3.90×10^{-6}
10							1.49×10^{-6}

TABLE 4b

SIMILARITY OF DIAGONAL ELEMENTS OF S_{ij}

	Average Value, $\bar{S}_\ell$	Average Deviation from $\bar{S}_\ell$ as a % of $\bar{S}_\ell$
S_1	1.00×10^{-4}	
S_2	1.37×10^{-4}	4%
S_3	9.08×10^{-5}	122%
S_4	3.02×10^{-5}	99%
S_5	1.83×10^{-5}	58%
S_6	1.31×10^{-5}	78%
S_7	6.28×10^{-6}	62%
S_8	3.68×10^{-6}	57%
S_9	2.00×10^{-6}	67%
S_{10}	1.17×10^{-6}	61%

Tables 5a and 5b show the results of the correlation given by each of these matrices compared to the measurements of the actual concentration obtained by holography. None of the matrices show results which in anyway resemble the actual concentrations. The difference in matrix elements between the three matrices used is not large, yet the difference in concentration values produced is very great, suggesting that the matrix-solving routine is highly sensitive to errors in the elements. This conclusion is strengthened by the observation that the corrected concentration values appear to get increasingly inaccurate as one goes from N_{10} to N_1, since this is the order in which the concentrations are solved for in the inversion scheme.

5.3.2 Correlation with Intensity Distributions

5.3.2.1 Comparison of intensity distributions. Since measurements of the actual PV intensity distribution were not made during the experiments involving microsphere distributions, another series of experiments was conducted to investigate this phenomenon. Figures 12 through 14 show the results of laser intensity profile measurements made on three separate occasions without changing the laser and optical arrangement. In each figure, part A shows the intensity profile at a location 2 to 3 feet from the laser light source, and part B shows it at about 6 feet away and after it has passed through a 1-inch thick plexiglas window and 6 inches of water. These distributions are shown normalized with respect to the peak intensity.

TABLE 5a

USING S_{ij} MATRICES TO CORRECT A RANDOM SIZE DISTRIBUTION OF NUCLEI - MIXTURE SPHERE SIZES

	Hologram	Actual Element	Column Element	Average Element
0	0.0	1.416×10^{7}	1.336×10^{7}	8.236×10^{4}
1	0.0	-1.641×10^{4}	-1.452×10^{4}	1.758×10^{1}
2	0.0	1.582×10^{4}	5.391×10^{3}	-1.318×10^{3}
3	0.0	-1.594×10^{3}	-2.869×10^{3}	-5.120×10^{1}
4	1.600×10^{4}	-3.550×10^{3}	1.454×10^{3}	2.623×10^{3}
5	0.0	-3.980×10^{3}	-1.050×10^{3}	7.353×10^{1}
6	1.468×10^{4}	4.903×10^{3}	9.973×10^{2}	-3.835×10^{3}
7	0.0	4.239×10^{2}	2.185×10^{2}	-3.640×10^{3}
8	0.0	5.050×10^{2}	2.414×10^{2}	1.061×10^{4}
9	3.221×10^{3}	2.315×10^{1}	2.905×10^{1}	-2.253×10^{3}
10	0.0	1.258×10^{1}	1.258×10^{1}	1.258×10^{1}

TABLE 5b

USING S_{ij} MATRICES TO CORRECT A RANDOM SIZE DISTRIBUTION OF NUCLEI - AIR BUBBLES IN THE ARL/PSU 12-INCH WATER TUNNEL

	Hologram	Actual Element	Column Element	Average Element
0	0.0	-3.381×10^{6}	2.273×10^{5}	7.713×10^{3}
1	1.441×10^{-1}	9.523×10^{3}	1.191×10^{4}	1.371×10^{2}
2	7.205	1.004×10^{4}	9.108×10^{3}	-1.056×10^{4}
3	3.602×10^{1}	3.962×10^{3}	1.345×10^{3}	-5.854×10^{2}
4	6.484×10^{1}	1.349×10^{3}	3.152×10^{3}	2.041×10^{4}
5	2.161×10^{1}	-3.696×10^{3}	-1.509×10^{3}	4.332×10^{2}
6	0.0	1.114×10^{4}	7.351×10^{2}	-3.015×10^{4}
7	0.0	5.279×10^{2}	4.632×10^{2}	-2.855×10^{4}
8	0.0	-4.604×10^{1}	7.185×10^{1}	8.312×10^{4}
9	0.0	-5.010×10^{1}	-6.287×10^{1}	-1.769×10^{4}
10	7.205	9.881×10^{1}	9.881×10^{1}	9.881×10^{1}

15	28	27	17	32	21	29	36	38	28	13	
15	35	42	35	42	41	45	50	62	62	35	
20	36	51	50	67	58	69	79	82	70	48	
32	66	68	75	81	88	86	88	87	78	50	
55	83	85	89	91	92	87	89	84	72	42	
65	90	91	87	90	85	80	87	87	75	52	
67	90	89	87	91	93	83	83	86	71	46	(A)
77	95	87	86	92	91	84	79	73	57	28	
79	91	90	91	83	79	83	83	80	14	42	
77	92	98	94	82	77	86	87	74	65	38	
71	90	100	98	86	87	84	79	64	54	35	
64	74	83	77	81	94	76	68	60	52	38	
46	61	51	47	61	60	52	46	40	35	17	
28	50	35	47	27	54	46	35	41	31	23	

6	12	18	20	22	35	34	37	45	62	65	69		
6	13	20	22	32	52	59	64	71	78	74	70	61	
12	10	22	47	44	53	61	70	84	87	83	76	65	
27	18	23	49	54	60	72	82	85	86	69	51	39	
27	40	54	56	68	81	89	89	75	59	54	40	57	
36	34	37	60	80	91	95	86	64	52	55	38	61	
35	19	34	69	85	95	100	91	68	64	59	44	56	(B)
19	17	27	42	68	81	84	75	65	64	56	52	49	
14	14	32	56	66	62	62	63	47	45	35	43	39	
22	18	16	34	60	69	66	50	40	31	34	24	20	
13	24	36	48	62	71	71	57	41	36	30	30	22	
8	10	16	22	38	46	49	44	34	31	22	21	17	
12	9	20	27	38	45	37	28	14	20	16	13	13	

Figure 12. Normalized Laser Beam Intensity Distribution Before Entering Test Section (A) and Inside Test Section (B), Obtained on 9/1/81.

0	3	8	9	9	7	10	0
2	69	100	97	95	91	97	20
2	65	98	97	96	93	98	21
2	63	98	97	96	97	99	21
2	60	99	94	96	97	98	23
2	53	98	95	96	97	97	21
1	41	93	92	92	95	95	24
0	0	2	3	2	3	3	0

Figure 13a. Normalized Laser Beam Intensity Distribution Before Entering Test Section, Obtained on 10/7/81.

28 28 28 23 28 33 32 40 45 44 45 43 45 42 34 30 32 39 48 54 55 57 54 41
30 33 34 40 41 41 40 42 41 43 43 41 43 40 39 43 47 51 57 61 59 49 50 47
35 41 45 48 52 54 51 48 47 43 46 43 39 35 38 46 52 57 57 57 63 55 43 48
43 50 51 52 61 63 65 61 57 55 52 46 39 37 39 43 47 51 52 53 59 63 52 49
48 57 57 61 67 71 76 74 71 68 61 44 33 36 48 46 45 41 43 49 54 56 52 50
47 51 57 64 71 77 80 77 78 77 69 57 60 61 63 63 61 61 59 56 59 57 52 53 48
43 47 51 59 68 75 77 77 80 80 77 70 74 77 81 77 73 73 72 69 64 61 51 48
45 51 45 56 65 73 76 78 81 80 76 82 86 88 88 84 78 77 77 77 70 61 53 40
44 47 45 55 60 65 68 62 80 84 86 89 91 91 91 90 86 80 77 78 74 61 48 35
44 45 52 59 61 64 65 69 80 86 89 89 89 89 85 85 84 80 74 73 72 60 44
45 43 48 54 59 65 70 70 79 88 92 92 91 88 82 80 80 80 71 60 61 52 38
53 44 48 56 65 72 76 78 84 93 98 98 94 84 76 69 71 71 61 48 45
52 46 51 61 73 75 75 77 77 89 97 100 97 91 81 69 66 65 59 45 40
40 47 58 68 79 82 80 78 78 88 95 98 98 94 87 80 72 72 69 54 35 31
39 50 60 68 78 82 83 81 78 82 89 94 94 94 91 86 82 80 76 65 47 39
35 52 58 64 73 80 82 84 81 82 84 88 89 89 85 82 84 81 78 68 54 46
25 44 61 58 60 68 74 81 81 80 80 81 81 80 78 78 79 75 75 69 52 38
37 43 60 61 55 57 65 75 78 76 73 67 63 66 66 72 72 69 65 53 32
47 42 58 63 61 55 55 61 74 76 68 56 49 56 64 67 69 65 57 40 23
44 43 40 55 63 57 45 44 54 63 57 47 44 44 52 57 58 56 46 30 24
34 40 38 34 47 55 51 39 38 41 42 40 43 43 41 51 52 41 34 35 32

Figure 13b. Normalized Laser Beam Intensity Distribution Inside Test Section, Obtained on 10/7/81.

0	0	0	1	1	1	1	1	0	0	0	0
0	0	0	1	2	1	2	1	1	0	0	0
0	0	0	6	6	7	7	4	4	1	0	0
1	2	19	94	98	98	97	91	87	38	2	1
1	2	21	95	99	100	97	93	88	40	3	1
1	2	22	97	99	100	97	94	87	38	3	1
1	3	22	97	97	98	97	92	86	37	3	1
1	2	20	92	92	93	92	88	81	34	2	1
0	1	16	84	86	86	86	82	75	27	2	0
0	0	4	40	43	45	43	44	36	8	0	0
0	0	0	2	2	3	2	2	1	0	0	0
0	0	0	0	1	1	1	1	0	0	0	0

Figure 14a. Normalized Laser Beam Intensity Distribution Before Entering Test Section, Obtained on 10/16/81.

2	1	3	3	6	14	23	30	39	32	21	10	9	9	7	7	9	14	14
3	4	3	3	9	9	25	24	27	24	11	12	11	10	8	5	11	9	15
6	8	6	8	7	11	16	14	29	29	10	14	11	14	5	3	5	5	11
8	9	14	16	14	16	9	15	31	32	15	20	19	19	4	3	8	11	2
7	9	14	21	18	20	12	29	22	20	27	32	17	11	5	3	9	7	2
10	12	23	22	23	32	32	44	35	27	39	37	11	7	5	3	5	5	5
11	14	23	23	34	37	50	51	32	27	45	42	14	22	9	9	5	6	5
12	10	20	18	35	37	52	55	45	41	43	38	25	27	16	14	7	9	4
10	11	18	16	36	38	55	56	55	50	43	33	23	27	18	13	9	7	4
10	8	11	14	36	38	54	50	59	58	40	32	29	28	12	12	12	12	4
8	9	9	18	37	43	45	50	59	58	39	45	26	23	11	18	13	9	4
7	9	13	18	43	52	65	74	68	67	59	59	35	32	19	21	10	5	3
9	11	18	18	51	59	81	87	88	82	68	73	41	43	24	36	12	9	3
12	14	18	25	59	68	90	95	97	94	82	78	51	59	56	59	16	21	4
16	14	22	22	68	73	96	98	100	98	84	78	61	62	65	63	30	30	8
15	14	30	31	70	75	97	99	99	99	83	79	64	63	63	60	37	37	12
13	15	25	27	70	73	94	95	94	95	81	74	62	59	60	52	35	32	12
9	9	18	18	60	58	86	83	82	90	73	60	56	50	47	38	31	18	11
6	7	9	11	47	40	65	60	64	72	60	51	42	32	31	20	13	7	8
11	11	7	8	22	24	45	59	98	54	51	46	24	24	16	12	15	17	6
12	12	9	10	19	22	47	50	57	52	52	49	15	13	16	13	19	17	5
7	5	7	5	15	16	44	48	57	58	50	45	20	12	10	9	20	14	4
4	6	5	7	9	12	41	42	58	57	39	36	15	12	17	9	11	7	4
10	14	14	17	16	23	44	46	53	55	32	29	23	19	7	5	5	6	2
16	14	20	20	18	23	44	43	49	52	25	24	28	23	7	9	5	2	3
18	19	23	23	17	16	36	33	38	42	22	19	24	18	15	10	3	2	5
15	15	25	23	12	10	26	27	19	30	17	15	13	12	6	3	3	2	3
18	14	22	19	15	16	25	29	16	11	23	16	5	2	4	5	2	2	2
10	10	14	9	12	16	33	36	28	21	15	10	7	6	6	9	6	5	4
11	12	9	7	16	27	33	38	33	29	20	12	9	5	5	10	11	6	4

Figure 14b. Normalized Laser Beam Intensity Distribution Inside Test Section, Obtained on 10/16/81.

It can be seen that the intensity distributions of part A are all very similar and quite uniform. However, the same cannot be said for their counterparts of part B. Figure 15 brings out the differences in these distributions more vividly by comparing all of them in terms of their maximum intensity gradient profiles. Such a profile illustrates the largest difference in illumination that a scatterer could experience by passing through any given portion of the PV, and thus is an indication of the PV's non-uniformity. The intensity gradient is the ratio of the difference in intensity across an interval to the mean intensity in that interval, and is expressed as a percentage of the mean intensity in the given interval.

5.3.2.2 Effect of optical components on intensity distribution. The occurrence of these differences in the intensity distributions suggested the possibility that optical components might be having an effect. It was observed that the beam began to depart from a uniform intensity distribution as the beam strayed from passing through the center of the lens system. In addition, it was found that the diffraction fringes around the beam could be eliminated through the use of a square aperture that was 50 μm x 50 μm, a discovery made through successive use of smaller and smaller apertures until the diffraction pattern was observed to disappear.

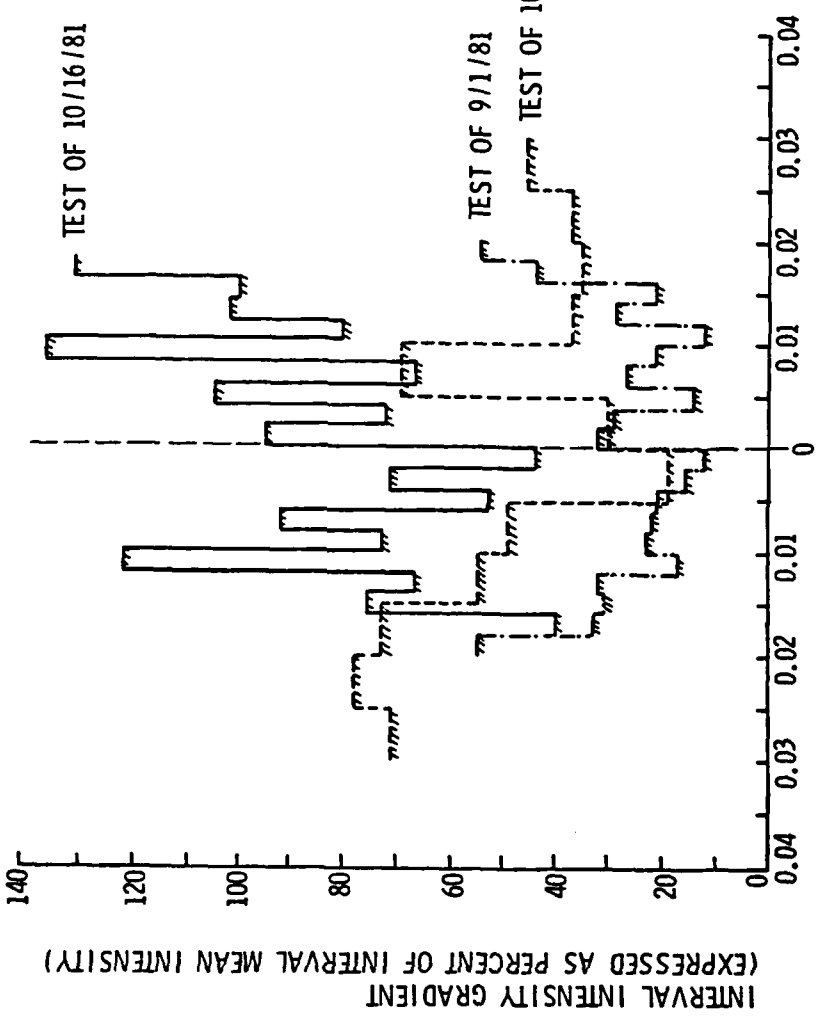

Figure 15. Comparison of Laser Probe Volume Intensity Distributions in Terms of Their Maximum Intensity Gradient Profiles.

CHAPTER 6

DISCUSSION OF RESULTS

6.1 Results of Coincidence Error Analysis

A very likely reason for the differences in coincidence error in the various tests is the difference in packaging concentration of calibration spheres. As was described in the experimental procedure, 24 μm marked the cutoff size where calibration spheres larger than this came 10^6 to a bottle, and sizes smaller than this came 10^7 to a bottle. This difference in the order of magnitude in the concentration is reflected in the difference of the level of coincidence error because each nuclei test used an entire bottle of calibration spheres.

The conclusion from these observations is that for the optical geometry and conditions of these experiments, the highest allowable nuclei concentration should be on the order of a 24-μm sphere concentration, i.e., about 1.5×10^4 per cubic inch, since concentrations greater than this result in coincidence probabilities greater than 20%.

In the analysis of the nature of coincidence errors given in Chapter 3, it was mentioned that the effect of nuclei coincidences in the PV could cause the PM-tube to interpret the event as a single large nuclei, so that one would expect that a nuclei distribution with a high coincidence probability would produce a PHA count rate distribution with a disproportionate number of counts in the higher channels. Table 1 indicates that the sphere mixture II was such a distribution, and Table 5a shows that the concentration calculated by matrix correction of the count rate distribution is indeed disproportionate,

predicting scatterers to be in higher size categories like 7, 8, and 10, where holography shows there to be none. Thus, coincidence errors could contribute to the inability of a given matrix to correct a count rate histogram.

6.2 Effectiveness of the Dual-Detector System

6.2.1 Non-Symmetric Particle Rejection. Kohler and Billet [12] predict that if a concentration of non-symmetric particles whose axial ratio is equal to 1.67 are analyzed by a dual-detector screening system with a cutoff asymmetry ratio set at $R_c = 0.75$, 84% of these particles are rejected by the system. If one interpolates between $R_c = 0.70$ and 0.80 in Table 2, one finds that the actual amount of dust particles rejected by the PHC in this investigation is 94%, indicating that the theory is actually conservative in its estimate of rejection ratio.

This conclusion is strengthened by the fact that the dust particles used in the investigation had an average axial ratio of less than 1.67, around 1.3. The theory predicts that as the axial ratio decreases, the amount of rejection should also decrease, for a given value of R_c in the PHC. Yet in actual performance, at an axial ratio of less than 1.67, the amount of rejection was still high.

6.2.2 Sphere Scattering Asymmetry. According to Table 3, the amount of rejection of spheres is higher than expected. As the cutoff rejection ratio, R_c, increases, so does the percentage of spheres rejected. In addition, this trend appears to be independent of size

and concentration, since all the tests show nearly the same amount of rejection for a given value of R_c.

One possible reason for this behavior of the spheres could be the influence of partial-illumination errors. In Section 3.2.4, it was described how the dual-detector system would screen out spheres which were illuminated non-uniformly, in addition to screening out non-uniformly shaped particles. However, the relationship between the non-uniformity of a sphere's illumination and the asymmetry of its scattered light intensity was not known.

Figure 15 gives an idea of the range of illumination non-uniformity that the spheres could experience in the PV. As an example, consider the plot corresponding to PV measurement of 10/16/81. Here, 72% of the PV width has a maximum illumination non-uniformity of greater than 70%, which means that nuclei passing through this PV would have a 72% chance of experiencing greater than 70% non-uniform illumination intensity. If it is assumed that 70% non-uniform illumination of a sphere results in 70% asymmetry in scattering intensity, then a PHC set at $R_c = 0.70$ would reject 72% of the nuclei passing through this PV. This figure is on the same order as the percentage of rejection of spheres at $R_c = 0.70$ in Table 3.

Measurements of the PV intensity distributions experienced by the spheres in each of the nuclei tests are not available. Nevertheless, this example should illustrate the fact that a high enough illumination non-uniformity can exist in a Probe Volume so that the kind of sphere rejection observed in Table 3 could result.

6.3 Effectiveness of the Matrix Method

Through observations on the performance of the matrix method shown in Tables 5a and 5b, it was concluded that the reason for the inability of the given matrices to correct the count rate data must be due to either or both of two sources. One possibility was that the actual PV intensity distribution (and, therefore, the S_{ij} matrix) experienced by the microspheres was different in each test, so that the S_{ij} matrix measured in one experiment would not correct count rate data from a different experiment. The other possibility considered was a problem of counting statistics; that is, a statistically insufficient number were counted in the tests. Physically, this would mean that the sample was not large enough during the measurement period to give a true picture of the PV intensity distribution; thus, the resulting S_{ij} matrix could not give a complete correction.

The information in Tables 6a and 6b gives significant insight into the influence of these various inaccuracies on the performance of the matrix method, especially the comparison of corrected count rate data from sphere mixture II given in Table 6b. The correction based on the new matrix elements represents elements which have been modified to account for the influence of the non-uniform PV illumination intensity. That the correction is better, yet still not sufficiently accurate, shows that the non-uniformity of the PV is not the only source of inaccuracy.

In Appendix C, section C.3, a description is given of a phenomenon referred to as the "aperture effect," which is shown to contribute to the inaccuracy of the matrix method correction.

TABLE 6a

COMPARISON OF COUNT RATES OBTAINED FROM EXPERIMENTS WITH COUNT RATES OBTAINED THROUGH THE INTENSITY MAPPING PROCEDURE

Classification Channel Number	1	2	3	4	5	6	7	8	9	10
Count Rate from Experiments (nuclei/second)	342	314	159	56	35	28	27	21	15	3
Count Rate from Intensity Mapping (nuclei/sound)	30	20	30	30	60	60	80	100	270	320

TABLE 6b

COMPARISON OF S_{ij} MATRIX ELEMENTS OBTAINED FROM EXPERIMENTS WITH MATRIX ELEMENTS OBTAINED THROUGH THE INTENSITY MAPPING PROCEDURE

S_ℓ	Column 10 Elements	Intensity Mapping Elements
S_1	1.06×10^{-4}	1.19×10^{-5}
S_2	1.33×10^{-4}	7.95×10^{-6}
S_3	4.63×10^{-5}	1.19×10^{-5}
S_4	2.50×10^{-5}	1.19×10^{-5}
S_5	1.97×10^{-5}	2.38×10^{-5}
S_6	1.42×10^{-5}	2.38×10^{-5}
S_7	1.02×10^{-5}	3.18×10^{-5}
S_8	5.84×10^{-6}	3.97×10^{-5}
S_9	3.90×10^{-6}	1.07×10^{-4}
S_{10}	1.49×10^{-6}	1.27×10^{-4}

CHAPTER 7

CONCLUSIONS

The modifications to the laser light scattering system developed by Keller have been shown to be valid and relevant means of solving inaccuracy problems in this system, insofar so they solve the inaccuracies they were designed to eliminate. The dual-detector method of distinguishing microbubble and solid particulate cavitation nuclei has been shown to exceed expectations for screening capability. Yet the usability of this method is limited by a different problem, that of spheres experiencing significant non-uniform illumination in the Probe Volume. It is believed that this is the primary cause of such a large percentage of spheres being rejected by the dual-detector system in addition to the non-symmetric particles.

The inversion scheme, or matrix method, of correcting the count rate data obtained from the light-scattering system's Pulse-Height Analyzer has been shown to be relevant to the problem of correcting for the distribution of light intensity in the PV, since the matrix of elements obtained from experiments conforms to the predicted equi-diagonal form. In addition, the intensity-mapping procedure of Appendix C showed that true values of the correction matrix, S_{ij}, could be calculated from direct measurements of the PV intensity profile.

This investigation also revealed another possible source of inaccuracy, that of insufficient count to produce a statistically accurate count rate distribution. Although the extent of this problem could not be determined, its evidence was seen in that the inversion

scheme, using matrix elements generated by the intensity-mapping procedure, could only partially correct a count rate distribution from a random nuclei size concentration.

CHAPTER 8

RECOMMENDATIONS FOR FURTHER RESEARCH

Before the dual-detector system can be used with confidence in actual cavitation tests, the problem of high rejection of spheres must be solved. An investigation should be conducted into the scattering response of a sphere to an incident beam with a gradient of light intensity, an investigation which should include a treatment of the Mie scattering equations for the case of a non-uniform plane wave incident upon a spherical particle. The results of such an investigation would be used to estimate the number of microbubble nuclei that would be rejected by a dual-detector system.

In terms of practical additional modifications, a mask could be placed over the photo-multiplier tube, using a square aperture instead of the slit aperture currently in use. Scans of the PV intensity distribution would reveal the region with the least non-uniformities, and the size and position of the aperture could be adjusted to examine only that region.

Concerning the problem of the statistics of nuclei counting, an investigation should be conducted as to how many nuclei must be measured in a given counting period to insure a statistically accurate sample. Factors like the nuclei size and the shape of the PV intensity profile should be examined, because the statistical size depends on any of these parameters.

CHAPTER 9

SUMMARY

This investigation has presented a combination of modifications to the laser light-scattering system designed by Keller [2], as a means of solving inaccuracy problems in the system and making it a reliable means of measuring nuclei. The two primary inaccuracy problems were the inability of the system to distinguish between microbubble and solid particulate nuclei and the persistent registering of nuclei in classification channels not representing their true size.

Theories were outlined which described the principles governing these inaccuracies, and modifications to the Keller system were proposed based on these theories. To facilitate the screening of solid particulate, or non-bubble nuclei from the total nuclei distribution being measured, a dual-detector signal analysis system was proposed based on a theory of scattering by non-symmetric particles in the Mie size range. To correct for inaccurate count rates reported by the system's Pulse-Height Analyzer, a mathematical technique called an inversion scheme was utilized. A formula for estimating the effect of errors due to nuclei coincidence was presented, based on the Poisson probability model.

A series of rigorous experiments was designed and implemented in order to test the effectiveness of these modifications. In these experiments, the light-scattering system (LSS) was used to measure nuclei distributions in a highly controlled environment, and a

holography system was used to calibrate the LSS test results. In this same series of experiments, microsphere distributions were tested to observe their response to various levels of discrimination in the dual-detector system.

When data from the experiments involving nuclei distribution failed to yield a matrix of elements for the inversion scheme that could successfully correct random nuclei distributions, a second series of experiments was conducted to investigate changes in the intensity profile of the Probe Volume.

In the process of analyzing the combined results of these experiments, another source of inaccuracy in the light-scattering system was encountered, which was the problem of the statistics of nuclei counting, or not measuring enough nuclei in a given counting period to give a statistically accurate count rate distribution. Evidence of the problem was discovered through the use of the intensity-mapping technique, which was introduced in this investigation as a means of determining the elements of the area matrix, S_{ij}, by direct measurement of the PV intensity profile. However, the means for eliminating this problem were not developed in this investigation.

The conclusion of the investigation was that both modifications to the Keller system were relevant to the inaccuracy problems observed, and that their capability of solving these inaccuracies has been proven, but that their usability in actual cavitation experiments would be limited until the problem of counting statistics and non-uniform illumination of spheres in the PV were solved. Recommendations were made for investigating these problems.

REFERENCES

1. Holl, J. W., "Nuclei and Cavitation," ASME Transactions, J. Basic Engineering, December 1970, pp. 681-688.

2. Morgan, W. B., "Air Content and Nuclei Measurements," Report of the 13th ITTC Cavitation Committee, 1972.

3. Keller, A. P., "The Influence of the Cavitation Nucleus on Cavitation Inception, Investigated with a Scattered Light Counting Method," ASME Transactions, J. Basic Engineering, December 1972.

4. Billet, M. L., and Gates, E. M., "A Comparison of Two Optical Techniques for Measuring Cavitation Nuclei," International Symposium on Cavitation Inception, ASME, New York, New York, December 1979.

5. Treaster, A. L., "Cavitation Hysteresis," M.S. Thesis, The Pennsylvania State University, June 1964, pp. 12-15.

6. Gates, E. M., et al., "Cavitation Inception and Nuclei Distributions - Joint ARL/CIT Experiments," CIT Technical Report No. E244.1, September 1979, p. 23.

7. Yungkurth, C. B., "Optimization of a Light-scattering System," B.S. Thesis, The Pennsylvania State University, May 1979.

8. Avellan, F., and Resch, F., "A Scattering Light Probe for the Measurement of Oceanic Air Bubble Sizes," International Journal of Multi-phase Flow, 1981.

9. Ling, S. C. and Gowing, S., "Measurements of Microbubbles in a Water Tunnel," 19th American Towing Tank Conference, University of Michigan, Ann Arbor, Michigan, July 1980.

10. Holve, D., and Self, S. A., "An Optical Particle-sizing Counter for In-situ Measurements," Technical Report for Project SQUID, Subcontract 8960-7, January 1978.

11. Keller, A. P., et al., "Comparative Investigations of the Scattered Light Counting Method for the Registration of Cavitation Nuclei and the Coulter Counter," Prepared for National Science Foundation, Michigan University, January 1974.

12. Kohler, R. A., and Billet, M. L., "Light Scattering by a Non-spherical Particle," Cavitation and Polyphase Flow Forum - 1981, ASME, Boulder, Colorado, June 1981.

13. (Reference to Duke Scientific microspheres - p. 20) Duke Scientific Corporation, 445 Sherman Avenue, Palo Alto, California, 94306.

14. Civil Engineering Department, Oklahoma State University, Stillwater, Oklahoma, 74047.

15. Vikram, Chandra S., Research Associate, Materials Research Laboratory, The Pennsylvania State University, private communications.

16. Gates, E. M., and Bacon, J., "A Note on the Determination of Cavitation Nuclei Distributions by Holography," SNAME J. Ship Research, Vol. 22, No. 1, March 1978

17. Van de Hulst, H. C., Light Scattering by Small Particles, New York, Wiley, 1957.

18. Kerker, M., Scattering of Light, New York, Academic Press, 1969.

19. Billet, M. L. Private Communications.

AD-A127 946 A LIGHT-SCATTERING SYSTEM TO MEASURE CAVITATION NUCLEI: 2/2
ANALYSIS AND CALI..(U) PENNSYLVANIA STATE UNIV
UNIVERSITY PARK APPLIED RESEARCH LAB.. C B YUNGKURTH
UNCLASSIFIED 30 SEP 82 ARL/PSU/TM-82-204 F/G 20/6 NL

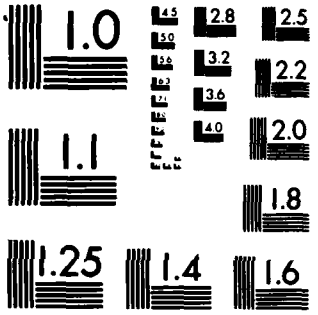

MICROCOPY RESOLUTION TEST CHART
NATIONAL BUREAU OF STANDARDS-1963-A

APPENDIX A

THEORETICAL DEVELOPMENT OF THE OPTIMUM MEASURING OPTICS LOCATION

The basis for a theoretical description of this light-scattering phenomenon comes primarily from the work of G. Mie in 1909 on the scattering of coherent light from spherical particles, as derived from Maxwell's equations of the electromagnetic character of light [17,18]. A brief summary of this development follows.

A.1 Mie Theory Derivation

The Mie theory of light scattering from a spherical particle arises from the solution of the scalar form of Maxwell's wave equation in spherical polar coordinates:

$$\frac{1}{\rho}\left[\frac{\partial^2(\rho\pi)}{\partial\rho^2}\right] + \frac{1}{\rho^2\sin\theta}\frac{\partial}{\partial\theta}\left[\sin\theta\,\frac{\partial\pi}{\partial\theta}\right] + \frac{1}{\rho^2\sin^2\theta}\frac{\partial^2\pi}{\partial\phi^2} + k^2\pi = 0, \qquad \text{(A.1)}$$

where π is a scalar component of a wave vector defined by the electric vector $\vec{E}$, and the magnetic vector, $\vec{H}$. Equation (2.1) is separable into three functions as

$$\pi = R(\rho)\,\Theta(\theta)\,\Phi(\phi)\,. \qquad \text{(A.2)}$$

The resulting equations are familiar ordinary differential equations which have the following solutions:

$$R(\rho) = \psi_n(k\rho) = \frac{\pi k\rho}{2}^{1/2} J_{n+1/2}(k\rho),\ \chi_n(k\rho) = \frac{\pi k\rho}{2}^{1/2}$$

$$= \frac{\pi k\rho}{2}^{1/2} N_{n+1/2}(k\rho) \qquad \text{(A.3)}$$

$$\Theta(\theta) = P_n^{(m)}(\cos\theta) \tag{A.4}$$

$$\Phi(\phi) = \sin(m\phi),\ \cos(m\phi) \tag{A.5}$$

where J and N are the half-integral order Bessel functions and $P_n^{(m)}$ are the Legendre polynomials, with the restriction that $-n \leq m \leq +n$.

The general solution for the scalar wave equation is then the linear superposition of all the particular solutions:

$$\rho\pi = \sum_{m=0}^{\infty} \sum_{m=-n}^{+n} [C_n\psi_n(k\rho) + d_n\chi_n(k\rho)]\,[P_n^{(m)}(\cos\theta)]\,[a_m\cos(m\theta) + b_m\sin(m\phi)] \quad . \tag{A.6}$$

In regards to the problem of scattering from a sphere, two cases must be represented: The equation of the incident wave and that of the scattered wave. A summation of the above expression over m gives these equations:

$$\rho\pi_1^{\,i} = \frac{1}{k^2} \sum_{n=1}^{\infty} i^{n-1}\,[(2n+1)/n(n+1)]\,\psi_n(k\rho)\,P_n^{(1)}(\cos\theta)\cos\phi \tag{A.7}$$

incident wave components

$$\rho\pi_2^{\,i} = \frac{1}{k^2} \sum_{n=1}^{\infty} i^{n-1}\,[(2n+1)/n(n+1)]\,\psi_n(k\rho)\,P_n^{(1)}(\cos\theta)\sin\phi \tag{A.8}$$

$$\rho\pi_1^{\,2} = -\frac{1}{k^2} \sum_{n=1}^{\infty} i^{n-1}\,[(2n+1)/n(n+1)]\,a_n\zeta_n(k\rho)P_n^{(k)}(\cos\theta)\cos\phi \tag{A.9}$$

scattered wave components

$$\rho\pi_2^s \approx -\frac{1}{k^2}\sum_{n=1}^{\infty} i^{n-1}\,[(2n+1)/n(n+1)]\,b_n\zeta_n(k\rho)P_n^{(1)}(\cos\theta)\sin\phi. \quad (A.10)$$

$\zeta_n(k\rho) = \psi_n(k\rho) + i\chi_n(k\rho)$ appears in the scattered wave expression because it vanishes at infinity, a necessary property of the scattered wave. In addition, the coefficients a_n and b_n (not to be confused with a_n and b_m) appear as the arbitrary factors which characterize the scattered wave. They are:

$$a_n = \frac{\psi_n'(y)\psi_n(x) - m\psi_n(y)\psi_n'(x)}{\psi_n'(y)\zeta_n(x) - m\psi_n(y)\zeta_n'(x)} \quad (A.11)$$

$$b_n = \frac{m\psi_n'(y)\psi_n(x) - \psi_n(y)\psi_n'(x)}{m\psi_n'(y)\zeta_n(x) - \psi_n(y)\zeta_n'(x)}\ ;\ m = \quad (A.12)$$

relative refractive index

where x = size parameter $= \frac{2\pi\rho}{\lambda}$; $y = mx$.

Because the function $\zeta(k\rho)$ vanishes at infinity, it can be approximated by a function of the type $e^{-ik\rho^*}$. Thus, one final simplifying change is made in the expressions for the scattered wave:

$$\rho\pi_1^s = \left(\frac{-i}{k\rho}\right) e^{-ik\rho}\sum_{n=1}^{\infty}[(2n+1)/n(n+1)2][a_n\pi_n(\cos\theta) + b_n\tau_n(\cos\theta)]\cos\phi \quad (A.13)$$

*Assuming that ρ is always measured in the far field.

and

$$\rho\pi_s^2 = \left(\frac{-i}{k\rho}\right) e^{-ik\rho} \sum_{n=1}^{\infty} [(2n+1)/n(n+1)] \; [b_n \pi_n(\cos\theta)$$

$$+ a_n \tau_n (\cos\theta)] \sin\phi, \tag{A.14}$$

where, for the purposes of calculation, π_n and τ_n are defined as

$$\rho_n(\cos\theta) = P_n^{(1)}(\cos\theta)/\sin\theta \tag{A.15}$$

$$\tau_n(\cos\theta) = \frac{d}{d\theta} [P_n^{(1)}(\cos\theta)] \; . \tag{A.16}$$

Now, the scattered electric field vector, and subsequently the scattered light intensity, may be defined.

The general form of the vector wave equation is

$$\vec{E} = A e^{iwt} \; . \tag{A.17}$$

Having obtained the scalar factor A from the solution of the scalar wave equation, the scattered components of the electric field can be expressed as:

$$\vec{E}_\theta = \left(\frac{1}{k\rho}\right) e^{i(wt-k\rho)} \cos\phi \; S_2(\theta) \tag{A.18}$$

and

$$\vec{E}_\theta = \left(\frac{-1}{k\rho}\right) e^{i(wt-k\rho)} \sin\phi \; S_1(\theta), \tag{A.19}$$

where $S_1(\theta)$ and $S_2(\theta)$ are known as the complex amplitudes of the scattered wave, and are defined as

$$S_1(\theta) = \sum_{n=1}^{\infty} [(2n+1)/n(n+1)2][a_n \pi_n(\cos\theta) + b_n \tau_n(\cos\theta)] \quad (A.20)$$

$$S_2(\theta) = \sum_{n=1}^{\infty} [(2n+1)/n(n+1)2][b_n \pi_n(\cos\theta) + a_n \tau_n(\cos\theta)]. \quad (A.21)$$

Intensity is defined by the square of the modulus of the electric field vector, $I = |\vec{E}|^2$. Thus, the total scattered intensity of light must be defined by the modulus of the vector sum of the components of

$$\vec{E},\ I = |E_\theta + E_\phi|^2 . \quad (A.22)$$

There is a phase difference between $\vec{E}_\theta$ and $\vec{E}_\phi$ given by

$$\tan\delta = \frac{\mathrm{Re}(S_1(\theta))\ I_m(S_2(\theta)) - \mathrm{Re}(S_2(\theta))\ I_m(S_1(\theta))}{\mathrm{Re}(S_1(\theta))\ \mathrm{Re}(S_2(\theta)) + \mathrm{Im}(S_2(\theta))\ \mathrm{Im}(S_1(\theta))} . \quad (A.23)$$

Thus the scattered components are:

$$\vec{E}_\theta = \left(\frac{i}{k\rho}\right) e^{i(wt-k\rho+\delta)} \cos\phi S_2(\theta) \quad (A.24)$$

and

$$\vec{E}_\phi = \left(\frac{-i}{k\rho}\right) e^{i(wt-k\rho)} \sin\phi S_1(\theta) . \quad (A.25)$$

These can be re-expressed in the following ways:

$$\vec{E}_\phi = \left(\frac{-1}{k\rho}\right) [e^{-i(k\rho-wt-\pi/2)}] \sin\phi S_1(\theta)$$

$$= \left(\frac{-1}{k\rho}\right) e^{iwt} [\sin(k\rho) - i\cos(k\rho)] \sin S_1(\theta) \quad (A.26)$$

and

$$\vec{E}_\theta = \left(\frac{1}{k\rho}\right) e^{iwt} [\sin(k\rho+\delta) - i\cos(k\rho+\delta)] \cos S_2(\theta). \quad (A.27)$$

Therefore, substituting Equations (A.25) and (A.26) into Equation (A.22) gives the final expression for the intensity as

$$I_{total} = \frac{1}{k^2\rho^2} \left| (\sin(k\rho) - i\cos(k\rho))\, \sin\phi S_1(\theta) - (\sin(k\rho+\delta) - i\cos(k+\delta))\cos\phi S_2(\theta) \right|^2 . \quad (A.28)$$

A.2 Characteristics of Mie-Scattered Light

It can be seen from section A.1 that, in general, this scattered light intensity can be summarized in function form as

$$I/I_0 = f(d, m, \rho, \theta, \phi, \lambda), \quad (A.29)$$

where I = scattered light intensity

I_0 = incident light intensity

d = spherical particle diameter

m = relative refractive index of particle with respect to medium

ρ = distance from particle location to intensity measurement location

θ,ϕ = solid angle into which light is scattered

λ = laser light wavelength.

This scattered light intensity shows a strong angular dependence, and it is because of this dependence that an optimum position (θ,ϕ) of the receiving optics was investigated.

APPENDIX B

SUMMARY OF THE INVERSION TECHNIQUE

B.1 Introduction

In the process of developing the ARL/PSU Laser Light-scattering System (LSS) for the measurement of microbubble and solid particulate in water, Reference [7] shows that such nuclei will scatter light in the manner predicted by the calculations of Mie in 1909. This was done by observing the response function of single particles as they passed through a beam of laser light. However, experience has consistently shown that when this same experimental technique is used to measure concentrations of nuclei in a continuous-flow situation, the technique fails to give an accurate representation of either the nuclei concentration or the nuclei size distribution.

In January of 1978, Holve and Self [10] were developing a similar LSS and encountered the same experimental difficulties. Their solution was to develop a numerical method of evaluating the nuclei counter data, based on a correction for the particle trajectory through different parts of the LSS measuring control volume. Mathematically, this correction can be described as follows.

Previous to this numerical scheme, the amplitude of the voltage pulse corresponding to a particle entering the measuring control volume (CV) was thought to be given by

$$A = G\, I_o\, F(\alpha, \Omega), \tag{B.1}$$

where A = voltage amplitude

G = gain of the photo-multiplier and associated electronics

I_o = intensity of the laser light in the CV

$F(\alpha,\Omega)$ = scattering response function

α = particle size parameter

Ω = solid angle into which light is scattered.

According to Holve and Self, Equation (B.1) should be modified to read

$$A = G\ I_o(y,z)\ H(y,z,\alpha)\ F(\alpha,\Omega), \tag{B.2}$$

where H = dimensionless function, varying between 0 and 1, describing the percentage of scattered light from the CV that reaches the PM,

and where I_o is now seen to be a function of the coordinates transverse to the flow direction (see Figure 3). It can be seen that Equation (B.2) will collapse to Equation (B.1) if the CV illumination intensity (I_o) is uniform, and if the transfer function (H) is equal to unity.

Similarly, it was previously known that the nuclei counting rate is related to the nuclei number density by

$$C_i = USN_i, \tag{B.3}$$

where C_i = nuclei counting rate

U = mean flow velocity

S = area of CV normal to U

N_i = nuclei number density.

Holve and Self modified Equation (B.3) to provide the matrix equation

$$C_i = US_{ij}\, N_j, \tag{B.4}$$

where $C_i = C(A_i)$ = column matrix of signal count rates for signal amplitudes in the range A_i to $a_i + \Delta A_i$

$N_j = N(F_j)$ = column matrix of nuclei number densities for nuclei in the size parameter range that yield normalized response functions in the range F_j to $F_j + \Delta F_j$

$S_{ij} = S(A_i, F_j)$ = equivalent cross-sectional area of the PV which yields normalized amplitudes in the range A_i to $A_i + \Delta A_i$ for particles having normalized response functions in the range F_j to $F_j + \Delta F_j$

i,j = indices referring to the channel number on the pulse-height analyzer (PHA).

The actual data received in a nuclei-counting experiment are the C_i collected in the channels of the PHA. The information desired is the nuclei number density, N_j, in each size range, j, of the PHA. Thus, Equation (B.4) is rewritten as

$$N_j = \frac{1}{U}\, C_i\, S_{ij}^{-1}, \tag{B.5}$$

where S_{ij}^{-1} = inverse of the matrix S_{ij} in Equation (1.4).

Thus, it can be seen from Equation (B.5) that the nuclei number density in one channel is actually a weighted sum of the count rates from every channel. This is the basic proposition of the numerical method of Holve and Self.

B.2 Determination of the Area Matrix

It is obvious from Section B.1 that the key to determining the nuclei number densities is the ability to determine the area matrix, S_{ij}. Recalling Equation (B.2), it can be seen that this area is related to the beam intensity and transfer function, and therefore it can have a dependence on particle size in the most general case.

Therefore, the most direct and the most certain method of determining the area matrix would proceed as follows. A monodisperse particle distribution of known size, d_k, and concentration, $N(d_k)$, is passed through the measurement volume at a known speed, U. Signal pulses are accumulated in the PHA for a specified length of time, yielding a count rate distribution, C_i. The matrix Equation (B.4) then reduces to

$$C_i = U\, S_{ik}\, N_k, \tag{B.6}$$

since N(dj) = 0 for all j, except j = k. Thus, Equation (B.6) will give all the i elements of column j = k of the S_{ij} matrix. The procedure is then repeated for the j size-range categories of the PHA.

This, however, can be a time-consuming project. Holve and Self have shown that this procedure can be greatly simplified if two criteria are met:

(1) The amplitude categories in the PHA are scaled logarithmically.

(2) The area function, specifically $H(x,z,\alpha)$, is independent of size parameter α.

However, given that the necessary criteria are met, the set of equations in Equation (B.6) reduced further to

$$C_i = U\, S_\ell\, N_m \tag{B.7}$$

$$S_\ell = \frac{1}{UN_m} C_i, \tag{B.8}$$

where N_m = concentration of a particle size, d_{max}, from the largest size class in the PHA.

The implication of Equation (B.8) is twofold. First, it implies that the form of the S matrix is such that all the elements on any diagonal are equal. Second, it implies that all the elements of the matrix, i.e., $\ell = 1, m$, can be determined from a single calibration experiment, using a concentration of a particle size d_m.

Once the elements of the S matrix have been determined, the only step remaining is to calculate its inverse, S_{ij}^{-1}. This should be a relatively simple matter, since S_{ij} will always be in upper-triangular form with non-zero elements.

For a given geometry and flow conditions of an experimental setup, this matrix need only be determined once. Thereafter, the nuclei concentrations may be calculated directly from the PHA count-rate data, according to Equation (B.5).

APPENDIX C

THE INTENSITY MAPPING PROCEDURE

C.1 Description of the Analysis

In Section 4.2.2.3, it was mentioned that measurements of a monodispersion of 70-μm spheres were made in conjunction with measurements of the Probe Volume (PV) intensity profile. These data were then used to make a comparison between the count rate distribution that was measured experimentally and the distribution that should have resulted according to the intensity profile that was measured experimentally.

Figure 16 demonstrates how an analysis referred to as the intensity mapping procedure was used to accomplish this comparison. This analysis assumes that a spatially uniform nuclei concentration of only one nuclei size (i.e., a monodispersion) is being measured and that all nuclei have an equal probability of sampling all portions of the PV.

Figure 16 is expressed in terms of normalized quantities. The right-side plot is the light-scattering calibration curve of Figure 1. Instead of nuclei size, the right-side abscissa is a fractional nuclei size, where the normalized nuclei size is expressed as a percentage of the monodispersion nuclei size. Likewise, the right-side ordinate is a normalized scattered light intensity. Considering the left-side plot, this is an intensity profile obtained by measurements of the laser light intensity at the center of the PV. The measurements were in a direction transverse to the direction of the incoming nuclei, a direction which is parallel to the beam's width. Thus the left-side

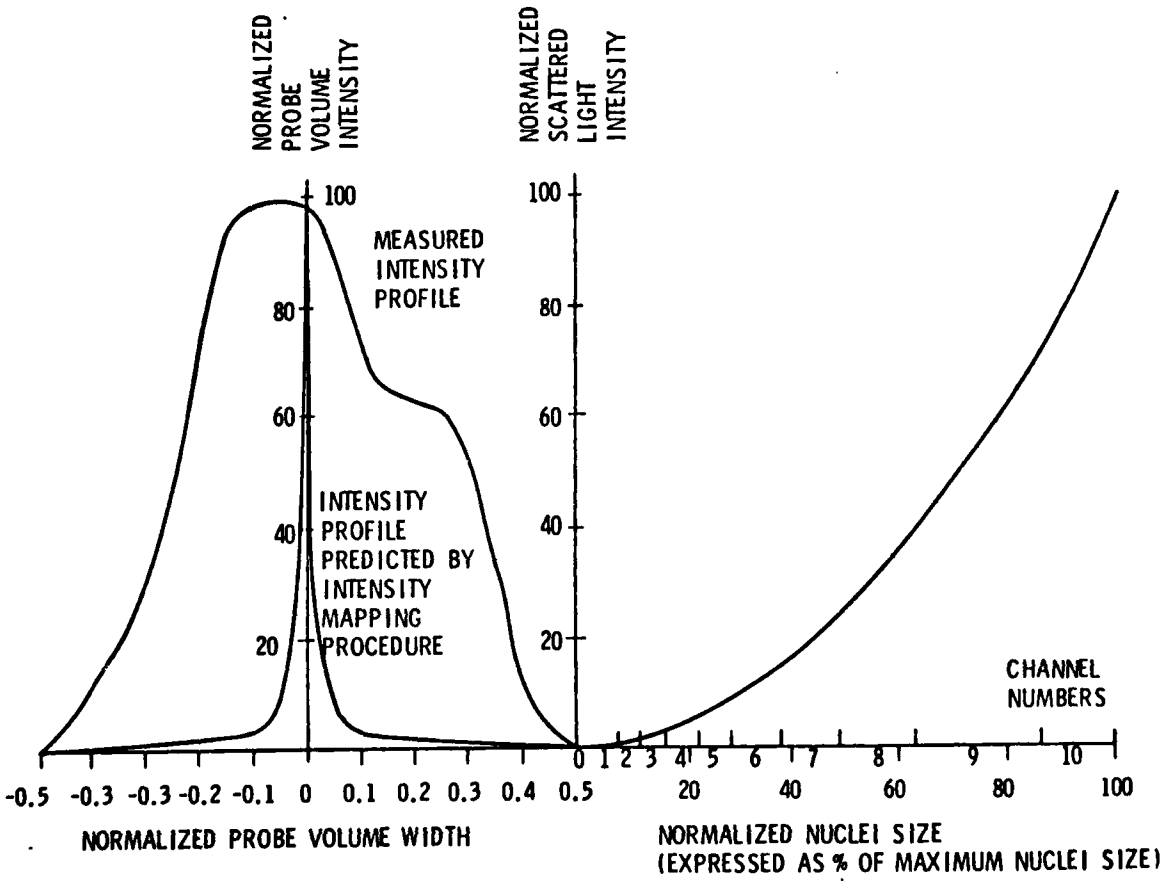

Figure 16. Method and Results of the Intensity Mapping Procedure.

abscissa is a normalized PV width. Since the assumption was made that all nuclei sample the PV equally, the abscissa takes on an additional meaning; namely, that a fraction of this PV width is equal to a fractional probability of nuclei sampling that portion of the PV width. Again, the ordinate of this curve is likewise a normalized intensity, where here the normalizing quantity is the peak laser light intensity in the PV.

Having defined the quantities in Figure 16, the intensity-mapping analysis proceeds as follows:

1. The nuclei classification channel divisions (as programmed into the PHA) are normalized by the monodispersion nuclei size. In this particular case, it is assumed that the experiment had a monodispersion of 70-μm spheres. The 70-μm size happens to be from the highest size category in the PHA, so that when the channel divisions are normalized, all 10 channel divisions will appear. Had the monodispersion corresponded to, for instance, the eighth size category, then when the channel divisions were normalized only channels 1 through 8 would have appeared on the right-side abscissa of Figure 16.
2. The calibration curve (right-side plot) relates a set of normalized nuclei size ranges to a set of normalized scattered light intensity ranges.
3. The set of normalized scattered light intensity ranges determine a set of normalized PV intensity ranges. There is an assumption here which can be expressed thusly: when

a nucleus is illuminated by some fraction of the PV peak intensity, the optical recording system "sees" this as a nucleus of some fraction of its true size being illuminated by the PV peak intensity.

4. The PV intensity profile relates a set of normalized PV intensity ranges to a set of fractions of the PV width.
5. The set of fractions of the PV width is equal to the set of probabilities of nuclei experiencing the set of normalized PV intensity ranges.
6. The set of probabilities gives the set of numbers of nuclei which experience the set of normalized PV intensity ranges.

C.2 Application of the Analysis

When the various physical quantities involved are considered in the way outlined by this intensity mapping analysis, the intensity-mapping procedure can be carried out in the order given above, or in a "reverse" order. In the order stated above, the analysis gives the number of nuclei which will appear in each classification channel out of a given sample size (like 1000 nuclei), for a known PV intensity distribution.

Table 6a gives the results of this analysis, compared to the actual distribution of counts in the classification channels that occurred for this experiment. In Table 6b the count rates obtained by this analysis are taken a step further through calculation of a set of equivalent matrix elements, S_ℓ, based on the experimental conditions that yielded the column 10 elements of Table 5. Finally, in Table 6c these data are taken yet another step further by using the

TABLE 6c

COMPARISON OF THE CORRECTION GIVEN BY EXPERIMENT MATRIX ELEMENTS WITH THE CORRECTION GIVEN BY INTENSITY MAPPING ELEMENTS

Corrected Sphere Mixture II (nuclei/in^3)

Concentration	From Intensity Mapping Elements	From Column 10 Elements	Holography Concentration Measurements
N_1	0.15	1.452×10^4	0.0
N_2	0.60	5.391×10^3	0.0
N_3	3.75	-2.869×10^3	0.0
N_4	8.94	1.454×10^3	1.600×10^4
N_5	24.37	-1.056×10^3	0.0
N_6	28.49	9.973×10^2	1.468×10^4
N_7	47.36	2.185×10^2	0.0
N_8	56.81	2.414×10^2	0.0
N_9	96.13	2.905×10^1	3.221×10^3
N_{10}	55.58	1.258×10^1	0.0

matrix elements of Table 6b to calculate a corrected sphere concentration distribution. Based on the count rate data obtained from the sphere mixture II experiment. It can be seen that the concentrations calculated with these equivalent matrix elements are more reasonable than those obtained with the matrix elements derived from the 70-μm sphere count rate measurements (i.e., the column 10 elements). Nevertheless, they still are not sufficiently accurate, as is seen when they are compared to the actual concentration data obtained through holographic measurements.

The procedure could also be performed in a "reverse" order; that is, an analysis which would show the PV intensity distribution that would produce a known distribution of nuclei in the PHA classification channels. Such an analysis was performed, and the result is the curve that appears to be approaching a delta-function on the left-side plot of Figure 16.

C.3 The Aperture Effect

Further experimental work done at ARL/PSU [19] has revealed yet another factor concerning the influence of the PV intensity distribution on the LSS's measurement accuracy. Specifically, it was observed that the PV intensity distribution was influenced by an "aperture effect," which can be visualized as follows.

As described in Section 2.1.2, the aperture placed over the photomultiplier tube restricts the length of the laser beam monitored by the measuring subsystem of the LSS; thus, the aperture defines the length of the PV. Previously, it was assumed that the aperture

produced a sharp definition of the PV length, so that nuclei passing through the portion of the beam monitored by the system were always counted, and nuclei passing through all other portions of the beam were never counted. The "aperture effect" observed at ARL/PSU showed that these PV boundaries set by the aperture were, in fact, not sharply defined. Therefore, there is a dim region around the PV that nuclei can pass through and still be monitored by the system; yet because of the decreased intensity, they will be counted by the system as being smaller than they actually are. In other words, there is an intensity profile in the length-wise direction of the PV as well as in the width-wise direction.

The impact of this aperture effect on the intensity-mapping procedure comes through step 4 of the analysis. Specifically, it means that, in reality, the PV intensity distribution relates a set of normalized PV intensity ranges to a set of fractions of the PV area, where this PV area is formed by boundaries of the PV width and the PV length. Thus, the number of nuclei in each classification channel is given by the relevant fraction of the PV area, not PV width.

Considering Figure 16 again, it can be seen that the effect here would be to use the left-side plot to become a two-dimensional intensity distribution, instead of simply a one-dimensional intensity profile. The intensity variation in the length-wise direction, due to the aperture effect, would be similar to the variation in the width-wise direction, having a peak intensity near the center and dropping off to zero at the extremes of the PV.

The effect of such a two-dimensional treatment of the intensity variation in the PV is predictable. More of the PV area will be related to low normalized intensity ranges, and less of the PV area will be related to high normalized intensity ranges. It then follows logically from the intensity-mapping procedure that more nuclei will be counted in the low size classification channels and less nuclei will be counted in the high size categories.

The trend of this effect is confirmed by the results of the experiments conducted, as seen in Table 6a. If the aperture effect influenced the counting and classification of nuclei in the way described above, then the "Count Rate From Intensity Mapping" (Table 6a) would shift toward a distribution of counts that looked more like the "Count Rate From Experiments," where the numbers of nuclei counted are large in the lower size categories.

DISTRIBUTION LIST FOR UNCLASSIFIED TM 82-204 by C. B. Yungkruth, dated 30 September 1982.

Commander
Naval Sea Systems Command
Department of the Navy
Washington, DC 20362
Attn: Library
Code NSEA-09G32
(Copy Nos. 1 and 2)

Naval Sea Systems Command
Attn: T. E. Peirce
Code NSEA-63R31
(Copy No. 3)

Naval Sea Systems Command
Attn: F. B. Peterson
Code NSEA-56X
(Copy No. 4)

Commander
David W. Taylor Naval Ship R&D Center
Department of the Navy
Bethesda, MD 20084
Attn: Library
Code 522
(Copy No. 5)

David W. Taylor Naval Ship R&D Center
Attn: T. T. Huang
Code 1552
(Copy No. 6)

Commanding Officer
Naval Underwater Systems Center
Newport, RI 02840
Attn: Library
Code 54
(Copy No. 7)

Commanding Officer
Naval Ocean Systems Center
San Diego, CA 92152
Attn: Library
(Copy No. 8)

Commander
Naval Surface Weapons Center
Silver Spring, MD 20910
Attn: Library
(Copy No. 9)

Defense Technical Information Center
5010 Duke Street
Cameron Station
Alexandria, VA 22314
(Copy Nos. 10 through 15)

Naval Research Laboratory
Washington, DC 20390
Attn: Library
(Copy No. 16)

Office of Naval Research
Department of the Navy
800 N. Quincy Street
Arlington, VA 22217
Attn: Director
(Copy No. 17)

The Pennsylvania State University
Applied Research Laboratory
Post Office Box 30
State College, PA 16801
Attn: GTWT Files
(Copy No. 18)

Applied Research Laboratory
Attn: J. W. Holl
(Copy No. 19)

Applied Research Laboratory
Attn: M. L. Billet
(Copy No. 20)

Applied Research Laboratory
Attn: D. R. Stinebring
(Copy No. 21)

Applied Research Laboratory
Attn: R. E. Henderson
(Copy No. 22)

Applied Research Laboratory
Attn: M. T. Pigott
(Copy No. 23)